Linear and Nonlinear Shear Wave Propagation in Viscoelastic Media

Brandon S. Lindley

A dissertation submitted to the faculty of the University of North Carolina at Chapel Hill in partial fulfillment of the requirements for the degree of Doctor of Philosophy in the Department of Mathematics.

Chapel Hill
2008

Approved by

Advisor: M. Gregory Forest
Reader: Richard M. McLaughlin
Reader: Sorin M. Mitran
Reader: Laura A. Miller
Reader: David B. Hill

ABSTRACT

BRANDON S. LINDLEY: Linear and Nonlinear Shear Wave Propagation in
Viscoelastic Media

(Under the direction of M. Gregory Forest)

This dissertation covers material pertaining to direct and inverse problems for vis-
coealstic materials with applications to pulmonary fluids (e.g. mucus) and other bi-
ological materials. This research extends a classic viscoelastic characterization tech-
nique, originally developed by John D. Ferry, to small volume (micro-liter) samples of
fluid through mathematical modeling and computation in the development of the micro-
parallel plate rheometer (MPPR). Ferry's inverse characterization protocol measures the
attenuation length and wave length of shear waves in birefringent synthetic polymers,
and uses the exact solution for a linear viscoelastic fluid undergoing periodic deformation
in a semi-infinite domain to obtain formulas relating these values to the linear viscoelastic
(material) parameters. In this dissertation, Ferry's exact solution is extended to include
both finite depth effects that resolve counter-propagating waves, and nonlinear effects
that arise from Giesekus and upper-convected Maxwell constitutive equations. These
generalizations of Ferry's solution are used in the development of the MPPR, which gen-
erates a shear wave in a finite depth domain and uses micro-bead tracking and nonlinear
regression on fluid displacement time series to extend Ferry's protocol of viscoelastic
characterization.

The final topic of this dissertation is a predictive model for stress communication and
filtering across viscoelastic layers. By focusing on stress signals arriving at either bound-
ary in a finite depth domain, this work identifies a remarkable structure in boundary

extreme stress signals which could play a key role in regulating certain aspects of lung function. This structure is derived from harmonic resonance in the elastic solid material limit, and demonstrated to persist and diverge from this limit as a function of a dimensionless parameter (the ratio of the attenuation length to the wave length). Analytical results demonstrate that this structure persists with respect to all material and driving parameters and in more general boundary value problems.

Dedicated in loving memory to Robert F. Hurst.

ACKNOWLEDGEMENTS

I would like to acknowledge the love and support of my family, especially my wife Candice, all of whom have stood behind me and encouraged me throughout this journey.

CONTENTS

LIST OF FIGURES

CHAPTER 1

Extensions of the Ferry Shear Wave Model

1.1. Introduction

The propagation of shear waves transverse to the direction of an imposed oscillatory shear at a non-slip boundary is a classic technique for linear viscoelastic characterization of non-Newtonian fluids (e.g. gels, polymers) [9, 10, 11]. In semi-infinite domain, the linear viscoelastic constitutive equations, coupled with momentum balance and boundary conditions, yield an exact solution [9]. John D. Ferry, whose original research extended Stokes' second problem for linear viscoelasticity, used strain-induced birefringence of synthetic polymers to image snapshots of propagating shear waves. From snapshots of these waves, the attenuation length and wavelength of the shear wave could be measured and, from the exact solution, the linear viscoelastic properties of the fluid determined.

This research lends itself naturally to the study mucociliary clearance in the respiratory tract, where cilia beating and tidal breathing propel airway surface liquid (ASL) along the respiratory tract up to the larynx. Applying the work of Ferry to even a first-order approximation of this problem, however, requires extending the model in several ways. First, the depth of the mucus/PCL layer is shallow enough to render the assumption of a semi-infinite domain invalid. Second, ASL (i.e. mucus) is regarded to be a non-linear viscoelastic fluid, exhibiting shear thinning and other properties incompatible with a linear viscoelastic model except at very low strains [6, 7]. Lastly, ASL is not a well characterized viscoelastic fluid, in part because obtaining samples is costly and time consuming. Thus, methods of viscoelastic characterization, such as Ferry's and others (e.g. cone and plate rheometery), must be extended for application to problems modeling mucociliary clearance.

The work of Mitran et al. [22] generalizes the exact solutions of Ferry to include finite depth effects, an upper convected nonlinearity, and also generates numerical solutions for non-linear models in the finite and semi-infinite domain. These generalizations lay the groundwork for a new method of inverse characterization (Chapter 2), as well as an exploration of the stress signals being communicated or filtered across a viscoelastic layer (Chapter 3).

1.2. Ferry's viscoelastic generalization of Stokes' 2nd problem

Consider the equations of motion for an incompressible fluid of density ρ,

$$(1.1) \qquad \rho\left(\frac{\partial \vec{v}}{\partial t} + (\vec{v} \cdot \nabla)\vec{v}\right) = \nabla \cdot \boldsymbol{T} + \rho \vec{g}$$

$$(1.2) \qquad \nabla \cdot \vec{v} = 0,$$

where $\vec{v}$ is the fluid velocity and $\boldsymbol{T}$ is the total stress tensor, the gradient of which is the sum total of forces acting within the fluid[1]. For our purposes, we negate the influence of gravity $\vec{g} \equiv \vec{0}$. The total stress tensor can be written as $\boldsymbol{T} = -pI + \boldsymbol{\tau}$ where p is the pressure, and $\boldsymbol{\tau}$ is called the "extra stress tensor." The extra stress tensor obeys a constitutive equation which describes the fluid's behavior to imposed stress or strain. In this case, the general linear viscoelastic constitutive law:

$$(1.3) \qquad \boldsymbol{\tau} = 2\int_{-\infty}^{t} G(t - t')\boldsymbol{D}(y, t')dt'.$$

Here $\boldsymbol{D}$ is the rate of strain tensor, given by,

$$(1.4) \qquad \boldsymbol{D} = 1/2(\nabla \vec{v} + \nabla \vec{v}^{\mathrm{T}}),$$

---

[1]Throughout this document, arrows will indicate column vectors, while bold symbols indicate tensors

and $G(t)$ is the shear relaxation modulus function. In general, no particular form is required of G, but it is worth noting that if G is a Dirac delta function $G(t) = \eta \delta(t)$,

$$(1.5) \qquad \boldsymbol{\tau} = 2 \int_{-\infty}^{t} \delta(t - t') \boldsymbol{D}(y, t') dt' = \eta \boldsymbol{D}(y, t),$$

then the equations for a viscous fluid, with kinematic viscosity η are recovered. For future reference, it is worth noting that for an exponential G,

$$(1.6) \qquad G(t) = G_0 e^{-(t/\lambda_0)},$$

one can obtain a differential form of (1.3) known as the single mode Maxwell constitutive equation. Here λ_0 is called the zero shear-rate relaxation time. This constitutive equation will be explored in depth in section 1.5.

Boundary Conditions and Analytical Solution.

Assume that the fluid sits in the upper half plane and that a non-slip plate located at $y = 0$ is oscillated at a single frequency in the x direction,

$$(1.7) \qquad v_x(0, t) = V_0 \sin(\omega t).$$

Here V_0 is the maximum velocity of the lower plate oscillation and ω is the frequency of the imposed oscillation. Also note that v_x indicates the x component of the velocity vector $\vec{v}$. A second boundary condition, imposing the velocity far away from the lower plate, is needed to form a well posed boundary value problem. The velocity far away from the plate must satisfy the boundary condition,

$$(1.8) \qquad \lim_{y \to \infty} v_x(y, t) = 0.$$

Note that the assumption of a single directional deformation and the semi-infinite geometry require that the only non-zero term of the velocity vector $\vec{v}$ is v_x and further that $\partial_x v_x(y, t) = 0$. Hence, the incompressibility condition (1.2) is satisfied. Further, the only non-zero stress term in the case of uni-directional shear, is the shear stress τ_{xy}. Thus,

the momentum equations and linear viscoelastic constitutive equation become:

$$(1.9) \qquad \frac{\partial v_x}{\partial t} = \frac{1}{\rho}\frac{\partial \tau_{xy}}{\partial y}$$

$$(1.10) \qquad \frac{\partial p}{\partial y} = 0.$$

In this geometry, the shear stress is given by,

$$(1.11) \qquad \tau_{xy}(y,t) = \int_{-\infty}^{t} G(t-t')\frac{\partial v_x}{\partial y}dt'$$

From (1.10) and (1.11), we derive a closed equation for v_x,

$$(1.12) \qquad \frac{\partial v_x}{\partial t} = \frac{1}{\rho}\int_{-\infty}^{t} G(t-t')\frac{\partial^2 v_x}{\partial y^2}dt'$$

This equation, together with the boundary conditions (1.7,1.8) is known to have an exact solution in the frequency locked limit, ignoring transients [9]. Consider the separable Fourier solution,

$$(1.13) \qquad v_x = \mathcal{I}m(\hat{v}_x(y)e^{i\omega t}).$$

From (1.12) we can write a simple ordinary differential equation for $\hat{v}_x(y)$,

$$(1.14) \qquad \frac{d^2\hat{v}_x}{dy^2} - \frac{i\rho}{\eta^*}\hat{v}_x = 0,$$

where we use the standard definition of the complex viscosity η^* [2],

$$(1.15) \qquad \eta^* = \int_0^{\infty} G(s)e^{-is}ds = \eta' - i\eta''.$$

The complex viscosity is a frequency dependant viscosity determined during forced harmonic oscillation. It represents the angle between the viscous stress and the shear stress, and is equal to the difference between the in phase component η', the dynamic viscosity, and the out of phase component η''. It is related to the complex shear modulus by the formula $G^* = i\omega\eta^*$.

The lower plate velocity (1.7) together with the decay condition (1.8) selects one independent solution of (1.14),

$$(1.16) \qquad \hat{v}_x(y) = V_0 e^{-\delta y},$$

where δ is given by,

$$(1.17) \qquad \delta = \sqrt{\frac{i\rho}{\eta^*}} = \alpha + i\beta,$$

and one can now write v_x as,

$$(1.18) \qquad v_x(y,t) = V_0 \mathcal{I}m(e^{i\omega t} e^{-\delta y}) = V_0 e^{-\alpha y} \sin(\omega t - \beta y).$$

Clearly, the attenuation length of the shear wave is given by α, and the wavelength of the shear wave is given by β, written in terms of the vicoelastic parameters,

$$(1.19) \qquad \alpha = \frac{\sqrt{\rho/2}}{|\eta^*|}\sqrt{|\eta^*| - \eta''}, \beta = \frac{\sqrt{\rho/2}}{|\eta^*|}\sqrt{|\eta^*| + \eta''}.$$

It is worth noting,

$$(1.20) \qquad \alpha^2 + \beta^2 = \frac{\rho}{|\eta^*|},$$

an identity which will be used later to write the shear stress in real variables.

The shear stress associated with (1.18) can now be found explicitly. From (1.11),

$$(1.21) \qquad \tau_{xy}(y,t) = \int_{-\infty}^{t} G(t - t') V_0 \mathcal{I}m(-\delta e^{i\omega t'} e^{-\delta y}) dt',$$

which can be rewritten,

$$(1.22) \qquad \tau_{xy}(y,t) = V_0 \mathcal{I}m\left(-\delta e^{-\delta y}\int_{-\infty}^{t} G(t - t') e^{i\omega t'} dt'\right),$$

and from the definition of η^*,

$$(1.23) \qquad \tau_{xy}(y,t) = V_0 \mathcal{I}m(-\delta \eta^* e^{i\omega t} e^{-\delta y}),$$

FIGURE 1.1. Exact solution for the semi-infinite geometry with $\eta_0 = 100$ g/ cm sec, $\lambda_0 = 1$ sec, $V_0 = 5$ cm/sec and $\omega = 1$ Hz.

an explicit solution for the shear stress is obtained. One can rewrite this as a real function, from equation (1.20),

$$(1.24) \qquad |\delta|^2 = \frac{\rho}{|\eta^*|},$$

and thus, the complex number δ rewritten,

$$(1.25) \qquad \delta = |\delta|e^{i\arg(\delta)} = \sqrt{\frac{\rho}{|\eta^*|}}e^{i\phi}.$$

Introducing the phase adjustment angle $\phi = \tan^{-1}(\beta/\alpha)$, we rewrite the shear stress as,

$$(1.26) \qquad \tau_{xy}(y,t) = V_0\sqrt{\rho|\eta^*|}e^{-\alpha y}\sin(\omega t - \beta y + \phi + \pi),$$

the real-valued definition of the shear stress. Figure 1.1 shows a typical viscoelastic shear wave in the semi-infinite domain for values $\eta_0 = 100$ g/cm sec, $\lambda_0 = 1$ sec, $V_0 = 5$ cm/sec and $\omega = 1$ Hz. These values will be used elsewhere to demonstrate viscoelastic properties.

1.3. Ferry's Protocol for Viscoelastic Characterization

The Ferry formula of viscoelastic characterization relies on measuring the physical attenuation length α and wavelength β in shear wave profiles obtained from birefringence patterns in synthetic polymers. To match the decay condition (1.8), a tank of the polymer must be deep enough, and (or) the shear wave amplitude small enough, that wave signals die out before reaching the upper interface and reflecting back in. Further, side walls of the the tank must be far enough away from the center that waves reflecting from the sides have died out before returning to the center of the chamber. Ferry details the results of calculations detailing these simplifications, and the associated errors, in [**10**] and [**11**]. Assuming reflecting waves from the top and side interfaces are not distorting the birefringence patterns in the chamber center, one can image the shear wave generated by oscillating the lower plate, and measure the physical quantities α and β. With these quantities, inversion of equation (1.19) will give the linear viscoelastic parameters η' and η'' for the polymer,

$$(1.27) \qquad \eta' = \frac{2\omega\alpha\beta}{\alpha^2 + \beta^2}, \eta'' = \frac{2\omega(\beta^2 - \alpha^2)}{\alpha^2 + \beta^2}.$$

1.4. Extensions of the Ferry Shear Wave Model for Finite Depth

The Ferry method of viscoelastic characterization relies on having enough polymer so that the waves mostly attenuate before reaching the upper interface. However, it is often not possible to obtain enough polymer for this to be a viable method of viscoelastic characterization. Further, the fluid chosen must admit birefringence patterns under oscillatory strain, limiting the types of fluids this method may be applied to. To overcome these limitation, a vast improvement is to generalize the method to use any volume, including a very small volume, of fluid and include the finite depth effects of the upper interface. Consider equation (1.14) coupled with the boundary conditions for oscillating upper and lower interfaces, where the fluid trapped in the upper half-plane between the

two interfaces at $y = 0$ and $y = H$,

(1.28)
$$v_x(0, t) = \mathcal{I}m(V_0 e^{i\omega t})$$

(1.29)
$$v_x(H, t) = \mathcal{I}m(V_H e^{i\omega t}).$$

Information about the relative phase difference between the two plates, as well as their amplitudes, is contained in the complex valued terms V_0 and V_H. The most obvious choice of boundary conditions will be to fix $V_0 \in \mathbb{R}$ and $V_H = 0$ which gives a fixed, non-slip upper plate combined with an oscillating lower plate as described in equation (1.7). The exact solution for the generic boundary value problem (1.28-1.29) is given by [22],

(1.30)
$$v_x(y, t) = \mathcal{I}m \left(V_0 e^{i\omega t} \frac{\sinh(\delta(H - y))}{\sinh(\delta H)} + V_H e^{i\omega t} \frac{\sinh(\delta y))}{\sinh(\delta H)} \right).$$

The shear stress is then given by,

(1.31)
$$\tau_{xy}(y, t) = \mathcal{I}m \left(-V_0 \delta \eta^* e^{i\omega t} \frac{\cosh(\delta(H - y))}{\sinh(\delta H)} - V_H \delta \eta^* e^{i\omega t} \frac{\cosh(\delta y))}{\sinh(\delta H)} \right).$$

Figure 1.2 Illustrates a shear wave in the finite depth geometry. The fluid parameters and driving conditions are identical to those used in Figure 1.1 with a stationary upper plate at $H = 10$ cm.

It is worth noting here that there is an equivalent stress controlled boundary value problem, i.e. one could impose stresses rather than strains (deformations) at either interface. The set of all well posed boundary value problems include boundary conditions that impose either a stress or strain at the lower and upper interface. Since the boundary value problems are equivalent, one could impose a particular velocity to get a predetermined shear stress, or solve for the velocity at either interface that is implied by imposing a controlled shear stress.

The formulas relating stress controlled to strain controlled experiments are quite straightforward. In order to impose a periodic shear stress of amplitude τ_0 at the lower
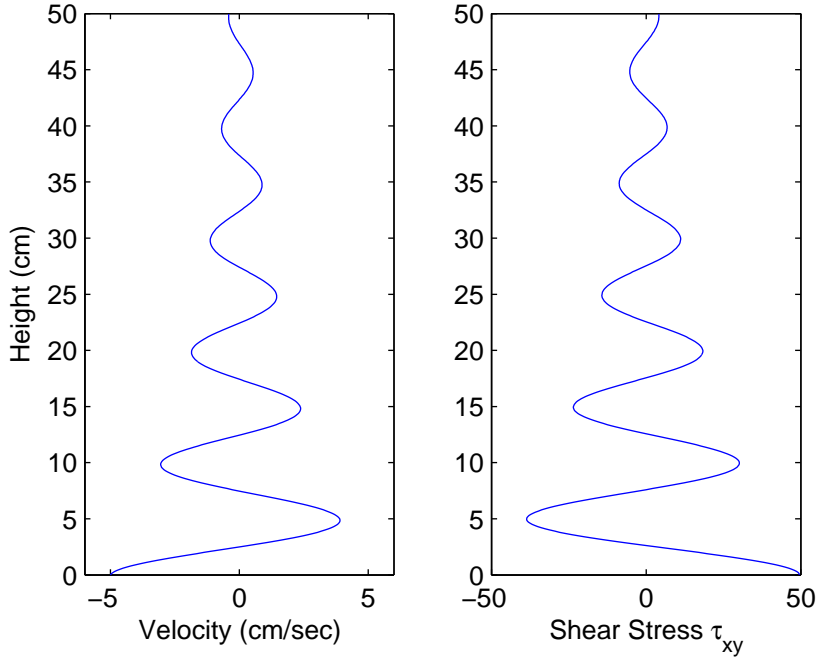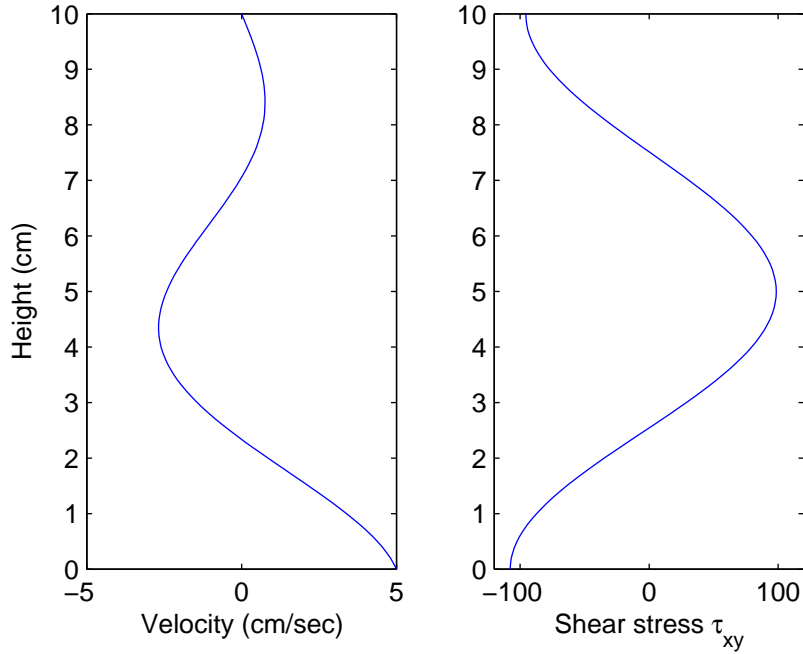
FIGURE 1.2. Exact solution for the finite depth geometry with $\eta_0 = 100$ g/cm sec, $\lambda_0 = 1$ sec, $V_0 = 5$ cm/sec $\omega = 1$ Hz, and $H = 10$ cm.

plate, the implied shear rate must satisfy the equation,

$$(1.32) \qquad\qquad V_0 \coth \delta H + V_H \mathrm{csch}(\delta H) = -\tau_0.$$

Likewise, a stress equivalent condition at the upper interface must satisfy,

$$(1.33) \qquad\qquad V_0 \mathrm{csch}(\delta H) + V_H \coth \delta H = -\tau_H.$$

Solving (1.32) and (1.33) with either V_0 or τ_0 known and either V_H or τ_H known gives an equivalent condition of the complementary type. Specific examples of these boundary value problems (with physical applications) will be given in Chapter 3.

Non-dimensional Coordinates.

To obtain non-dimensional coordinates for the models above, we choose the physical parameters as reference values. The reference viscosity is the zero strain-rate viscosity η_0 of the fluid. The reference length is the shear deformation amplitude A. The reference time ω^{-1} is set by the plate frequency. The reference stress is $\eta_0 \omega$, the viscous shear

stress at the lower plate. With these choices, the non-dimensional velocity of the bottom plate is now given as $\tilde{v}_x = \sin(\tilde{t})$, where the tilde superscript indicates non-dimensional quantities. The following non-dimensional quantities arise in the model equations and their solutions:

- Reynolds number $Re = \rho \omega A^2 / \eta_0$,
- Deborah number $De = \lambda \omega$,
- Bulk shear strain $\gamma = A/H$.

In these non-dimensional variables, the Ferry semi-infinite domain solution is,

$$(1.34) \qquad \tilde{v}_x(\tilde{y}, \tilde{t}) = e^{-\tilde{\alpha}\tilde{y}} \sin(\tilde{t} - \tilde{\beta}\tilde{y}),$$

with, $\tilde{y} = y/H$, $\tilde{t} = \omega t$. In these coordinates,

$$(1.35) \qquad \tilde{\delta} = \tilde{\alpha} + i\tilde{\beta} = \sqrt{iRe/\tilde{\eta}^*},$$

and,

$$(1.36) \qquad \tau_{xy}(\tilde{y}, \tilde{t}) = V_0\sqrt{Re|\tilde{\eta}^*|}e^{-\alpha y} \sin(\tilde{t} - \tilde{\beta}\tilde{y} + \tilde{\phi} + \pi).$$

The finite depth solution in non-dimensional coordinates follows logically.

1.5. Extensions of the Ferry Shear Wave Model for Nonlinearity

To extend this shear wave model to account for nonlinear viscoelastic behavior, we redefine the extra stress tensor $\boldsymbol{\tau}$ using a single-mode Giesekus constitutive model,

$$(1.37) \qquad \lambda_0 \overset{\triangledown}{\boldsymbol{\tau}} + \boldsymbol{\tau} + \mu(\boldsymbol{\tau} \cdot \boldsymbol{\tau}) = 2\eta_0 \boldsymbol{D}.$$

Where λ_0 denotes the relaxation time of the fluid, and η_0 denotes the zero-shear rate viscosity of the fluid. The coefficient μ denotes the mobility parameter, a non-dimensional

parameter derived from molecular dynamics that models shear-thinning, a common feature of viscoelastic polymers. The upper triangle $\overset{\triangledown}{\boldsymbol{\tau}}$ denotes the upper convected derivative given by [16],

$$(1.38) \qquad \overset{\triangledown}{\boldsymbol{\tau}} = \frac{\partial \boldsymbol{\tau}}{\partial t} + (\nabla \cdot \vec{v})\boldsymbol{\tau} - \nabla v^T \cdot \boldsymbol{\tau} - \boldsymbol{\tau} \cdot \nabla v$$

The upper convected derivative is necessary in this case (and for many applications in continuum mechanics) because it satisfies the property of invariance under scaling and rotation of coordinates [2, 16]. Under the assumption of a one-dimensional deformation in the x direction, the momentum equations become,

$$(1.39) \qquad \frac{\partial v_x}{\partial t} = \frac{1}{\rho}\frac{\partial \tau_{xy}}{\partial y}$$

$$(1.40) \qquad \frac{\partial p}{\partial y} = \frac{\partial \tau_{yy}}{\partial y}.$$

and the constitutive equation reduces to,

$$(1.41) \qquad \lambda_0 \dot{\tau}_{xx} - 2\lambda_0 \frac{\partial v_x}{\partial y}\tau_{xy} + \tau_{xx} + \mu(\tau_{xx}^2 + \tau_{xy}^2) = 0$$

$$(1.42) \qquad \lambda_0 \dot{\tau}_{xy} - \lambda_0 \frac{\partial v_x}{\partial y}\tau_{yy} + \tau_{xy} + \mu(\tau_{xx}\tau_{xy} + \tau_{xy}\tau_{yy}) = \eta_0 \frac{\partial v_x}{\partial y}$$

$$(1.43) \qquad \lambda_0 \dot{\tau}_{yy} + \tau_{yy} + \mu(\tau_{xy}^2 + \tau_{yy}^2) = 0.$$

The case of $\mu = 0$ reduces this system further, and is known as the single-mode upper convected Maxwell constitutive model. In the frequency locked response, the equations above reduce to,

$$(1.44) \qquad \frac{\partial v_x}{\partial t} = \frac{1}{\rho}\frac{\partial \tau_{xy}}{\partial y}$$

$$(1.45) \qquad \frac{\partial p}{\partial y} = 0$$

$$(1.46) \qquad \lambda_0 \dot{\tau}_{xx} - 2\lambda_0 \frac{\partial v_x}{\partial y} \tau_{xy} + \tau_{xx} = 0$$

$$(1.47) \qquad \lambda_0 \dot{\tau}_{xy} + \tau_{xy} = \eta_0 \frac{\partial v_x}{\partial y}$$

Interestingly, equations (1.44) and (1.45) for the velocity and pressure are precisely the equations given in the linear viscoelastic model. Further, equation (1.47) can also be obtained by substituting the exponential function $G(t) = \eta_0/\lambda_0 e^{-t/\lambda_0}$ into equation (1.3) and expanding. Note that the τ_{xx} term does not occur in the evolution equations for the velocity or the shear stress, so these velocity and stress equations can be solved independently of τ_{xx}. Thus, the single mode Maxwell model is equivalent to the linear viscoelastic problem, except that it includes an additional stress term, τ_{xx}. This means the exact solution of this problem is identical to the solution given in section 1.2, where the viscoelastic parameters η_0 and λ_0 are related to the linear viscoelastic parameters η' and η'' by,

$$(1.48) \qquad \eta' = \frac{\eta_0}{1 + (\omega\lambda_0)^2}$$

$$(1.49) \qquad \eta'' = \frac{\eta_0 \omega \lambda_0}{1 + (\omega\lambda_0)^2}.$$

Thus, in this simplest nonlinear model, the signature of nonlinearity is the additional stress term τ_{xx}, a measurable physical quantity, for which we obtain an integral solution dependent upon the exact solution for v_x and τ_{xy},

$$(1.50) \qquad \tau_{xx}(y, t) = 2 \int_0^t e^{(t'-t)/\lambda_0} \frac{\partial v_x}{\partial y}(y, t') \tau_{xy}(y, t') dt'.$$

The Giesekus model is fully nonlinear and, therefore, must be approached numerically.

Hyperbolic Structure and Numerical Solution.

To formulate a numerical procedure, we begin by rewriting the evolution equations (1.39-1.43),

(1.51)
$$\vec{q}_t = A\vec{q}_y + \psi(q),$$

where,

(1.52)
$$\vec{q} = \begin{pmatrix} v_x \\ \tau_{xx} \\ \tau_{xy} \\ \tau_{yy} \end{pmatrix}$$

(1.53)
$$A = \begin{pmatrix} 0 & 0 & \dfrac{1}{\rho} & 0 \\ 2\tau_{xy} & 0 & 0 & 0 \\ \tau_{yy} + \dfrac{\eta_0}{\lambda} & 0 & 0 & 0 \\ 0 & 0 & 0 & 0 \end{pmatrix}$$

(1.54)
$$\psi = -\frac{1}{\lambda} \begin{pmatrix} 0 \\ \tau_{xx} + \mu(\tau_{xx}^2 + \tau_{xy}^2) \\ \tau_{xy} + \mu(\tau_{xx}\tau_{xy} + = \tau_{xy}\tau_{yy}) \\ \tau_{yy} + \mu(\tau_{xy}^2 + \tau_{yy}^2) \end{pmatrix}.$$

The eignevalues of A are,

(1.55)
$$\lambda_1 = \lambda_2 = 0, \lambda_3 = -c, \lambda_4 = c$$

where c is the wave propagation speed,

(1.56)
$$c = \sqrt{\frac{\tau_{yy} + \eta_0/\lambda_0}{\rho}}.$$

Note that, in the upper-convected Maxwell model, the nonlinear terms vanish and c is constant, and thus we identify the zero shear rate wavespeed as,

$$(1.57) \qquad c_0 = \sqrt{\frac{\eta_0/\lambda_0}{\rho}}.$$

The associated right eigenvectors are,

$$(1.58) \qquad R = (r_1, r_2, r_3, r_4) = \begin{pmatrix} 0 & 0 & -c & c \\ 0 & 1 & 2\tau_{xy} & 2\tau_{xy} \\ 0 & 0 & c^2\rho & c^2\rho \\ 1 & 0 & 0 & 0 \end{pmatrix}.$$

Considering a local linearization of A where average values are used,

$$(1.59) \qquad \bar{R} = \begin{pmatrix} 0 & 0 & -\bar{c} & \bar{c} \\ 0 & 1 & 2\bar{\tau}_{xy} & 2\bar{\tau}_{xy} \\ 0 & 0 & \bar{c}^2\rho & \bar{c}^2\rho \\ 1 & 0 & 0 & 0 \end{pmatrix}, \quad \bar{R}^{-1} = \frac{1}{\bar{c}^2}\begin{pmatrix} 0 & 0 & 0 & 2\bar{c}^2 \\ 0 & 2\bar{c}^2 & -4\bar{\tau}_{xy}/\rho & 0 \\ -\bar{c} & 0 & 1/\rho & 0 \\ \bar{c} & 0 & 1/\rho & 0 \end{pmatrix},$$

where the overbars indicate locally averaged quantities. Now A can be rewritten locally as:

$$(1.60) \qquad A = \bar{R}\Lambda\bar{R}^{-1},$$

where,

$$(1.61) \qquad \Lambda = \begin{pmatrix} 0 & 0 & 0 & 0 \\ 0 & 0 & 0 & 0 \\ 0 & 0 & -\bar{c} & 0 \\ 0 & 0 & 0 & \bar{c} \end{pmatrix}$$

This linearization allows us to write (1.51) in characteristic variables,

$$(1.62) \qquad \frac{\partial \vec{w}}{\partial t} + \Lambda\frac{\partial \vec{w}}{\partial y} = \tilde{\psi},$$

14

and since Λ is diagonal, the system is now linear. Here, the characteristic variables are,

$$(1.63) \qquad \vec{w} = \begin{pmatrix} w_1 \\ w_2 \\ w_3 \\ w_4 \end{pmatrix} = \bar{R}^{-1}\vec{q} = \begin{pmatrix} \tau_{yy} \\ \tau_{xx} - 2\bar{\tau}_{xy}/(\bar{c}^2\rho)\tau_{xy} \\ -v_x/2\bar{c} + \tau_{xy}/(2\bar{c}^2\rho) \\ v_x/2\bar{c} + \tau_{xy}/(2\bar{c}^2\rho) \end{pmatrix},$$

and $\tilde{\psi}$ is,

$$(1.64) \qquad \tilde{\psi} = \bar{R}^{-1}\psi = \frac{1}{\lambda_0}\begin{pmatrix} \tau_{yy} + \mu(\tau_{xy}^2 + \tau_{yy}^2) \\ \tau_{xx} + \mu(\tau_{xy}^2 + \tau_{xx}^2) - 4\bar{\tau}_{xy}\sigma \\ \sigma \\ \sigma \end{pmatrix}, \sigma = \frac{\tau_{xy}}{2\bar{c}^2\rho}(1 + \mu(\tau_{xx} + \tau_{yy})).$$

One can revert to primitive variables, or rewrite $\tilde{\psi}$ in characteristic variables, by using the transformation,

$$(1.65) \qquad \vec{q} = \bar{R}w = \begin{pmatrix} \bar{c}(w_4 - w_3) \\ w_2 + 2\bar{\tau}_{xy}(w_3 + w_4) \\ \bar{c}^2(w_3 + w_4)\rho \\ w_1 \end{pmatrix}.$$

Any well posed boundary value problem must impose the positive eigenvalue characteristics (w_4) at the lower interface $y = 0$, and the negative eigenvalue characteristics (w_3) at the upper interface, $y = H$. Since these characteristics are a linear combination of v_x and τ_{xy}, then either one of v_x or τ_{xy} must be imposed independently at each boundary. The non-imposed value must be solved for as part of a numerical algorithm at each time step. Further, no special assumption is made about v_x or τ_{xy}, since we are no longer solving in fixed frequency domains using Fourier methods. Thus, arbitrary functions can be imposed at either interface for either the velocity or shear stress, including non-periodic

and even discontinuous functions (since wave propagations methods will be used to solve this system and these handle discontinuous data i.e. shocks, very well).

High Resolution Numerical Algorithm.

Exact solutions for the fully nonlinear Giesekus constitutive model do not exist, and so numerical methods are employed. Summarized below are techniques developed in [18] and [22] for numerical packages available online [17] and [24], although more primitive codes (and perhaps user friendly) are available as Matlab scripts [2]. The evolution equation can be rewritten as,

$$(1.66) \qquad \vec{q_t} = (\mathcal{A} + \mathcal{B})q, \mathcal{A} = -A(\vec{q})\frac{\partial}{\partial x}, \mathcal{B} = \psi(\vec{q}),$$

where $\mathcal{A}$ is the convective operator and $\mathcal{B}$ is the source term operator. Equation (1.66) is broken into two stages using Strang splitting,

$$(1.67) \qquad \vec{q}(t + \Delta t) = e^{(\mathcal{A}+\mathcal{B})\Delta t}\vec{q}(t) \approx e^{\mathcal{B}\Delta t/2}e^{\mathcal{A}\Delta t}e^{\mathcal{B}\Delta t/2}\vec{q}(t).$$

The source term of the operator is $\vec{q_t} = \mathcal{B}\vec{q}$, a system of ODE's which is advanced in time using a second-order Runge-Kutta scheme. The convective operator, $\vec{q_t} - \mathcal{A}q = 0$ is solved using wave propagation methods, where jumps between values adjacent cells are represented as propagating waves. Consider a uniform discretization of the interval $[0, H]$ with step size h of the finite depth shear wave problem. The cell center coordinates are $y_j = (j - 1/2)h$ for $j = 1, 2, ..., m$ and the cell edge coordinates are $y_{j-1/2} = (j-1)h$, $j = 1, 2, ..., m + 1$, with $h = H/m$. The cell finite volume average is,

$$(1.68) \qquad Q_j^n = \frac{1}{h}\int_{y_j - 1/2}^{y_j + 1/2} \vec{q}(y, t^n)dy.$$

---

[2]First and second order Matlab scripts for solving this problem are available via personal contact with the author blindley@email.unc.edu

The jump at the $j-1/2$ interface $\Delta Q^n_{j-1/2}$, is decomposed on the eigenbasis $\bar{R} = R((Q^n_j + Q^n_{j-1})/2)$,

$$(1.69) \qquad \Delta Q^n_{j-1/2} = Q^n_j - Q^n_{j-1} = \sum_{l=3}^{4} p^l_{j-1/2} r^l_{j-1/2},$$

$$(1.70) \qquad \mathcal{W}^l_{j-1/2} = p^l_{j-1/2} r^l_{j-1}, l = 3, 4.$$

Note that only the r_3 and r_4 eigenmodes are propagating, and hence $n_w = 2$ waves $\mathcal{W}^{3,4}_{j-1/2}$ are required. The p coefficients required are,

$$(1.71) \qquad p^3_{j-1/2} = \frac{\Delta Q_{3,j-1/2}}{2\bar{c}^2_{j-1/2}\rho} - \frac{\Delta Q_{1,j-1/2}}{2\bar{c}^2_{j-1/2}}, p^4_{j-1/2} = \frac{\Delta Q_{3,j-1/2}}{2\bar{c}^2_{j-1/2}\rho} + \frac{\Delta Q_{1,j-1/2}}{2\bar{c}^2_{j-1/2}}$$

where Q_1 and Q_3 are the 1,3 components of Q. Cell averaged values are now updated by,

$$(1.72) \qquad Q^{n+1}_j = Q^n_j - \frac{\Delta t}{h}\left(\mathcal{W}^4_{j-1/2} + \mathcal{W}^3_{j+1/2}\right),$$

plus second order correction [18]. The method is adaptive and second order in space and time. The convergence rates of this algorithm are demonstrated in [22] and packages available online [24, 17]. Figure 1.3 shows a shear wave snapshot (with stress terms) generated by this code at $t = 20.25$ for fluid parameters and driving conditions/depth corresponding to values in Figure 1.2. Here the Giesekus parameter is $\mu = .01$, and enough time steps were taken to allow transients to pass.

Convergence to Frequency Locked Response.

Figure 1.4 demonstrates the numerical method converging in time to the exact solution. Recall that the exact solution, (1.30) with (1.31), for the single mode Maxwell Fluid was obtained under the assumption that transients had passed. The numerical method above captures the onset and decay of these transients, and shows that the numerical solution converges to the frequency-locked response (exact solution) relatively quickly. Figure 1.5 illustrates the same features of Figure 1.4, now with respect to τ_{xx} or the first
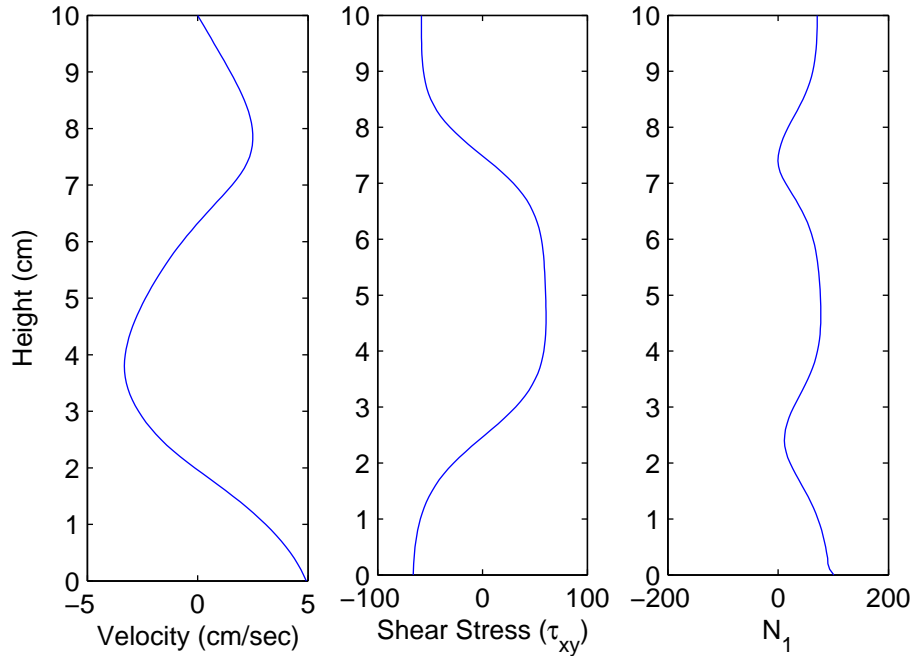
FIGURE 1.3. Numerical solution for the finite depth geometry for a Giesekus model fluid with $\eta_0 = 100$ g/cm sec, $\lambda_0 = 1$ sec, $\mu = .01$, $V_0 = 5$ cm/sec and $\omega = 1$ Hz, and $H = 10$ cm .

normal stress difference $N_1 = \tau_{xx} - \tau_{yy}$ since $\tau_{yy} = 0$ in the frequency-locked response.

1.6. Conclusion

Because of inherent limitations of the Ferry modeling and inverse characterization protocols, it was necessary to extend the Ferry shear wave model to include finite depth and nonlinear effects. With the development of these modeling tools, new protocols for inverse characterization have been developed in the form of a Micro-Parallel Plate Rheometer (MPPR), developed at UNC. This device imposes velocity controls at both surfaces in a parallel plate geometry, for which we have developed exact solutions. The construction, experimental, and modeling protocols for this device are covered in the following chapter.
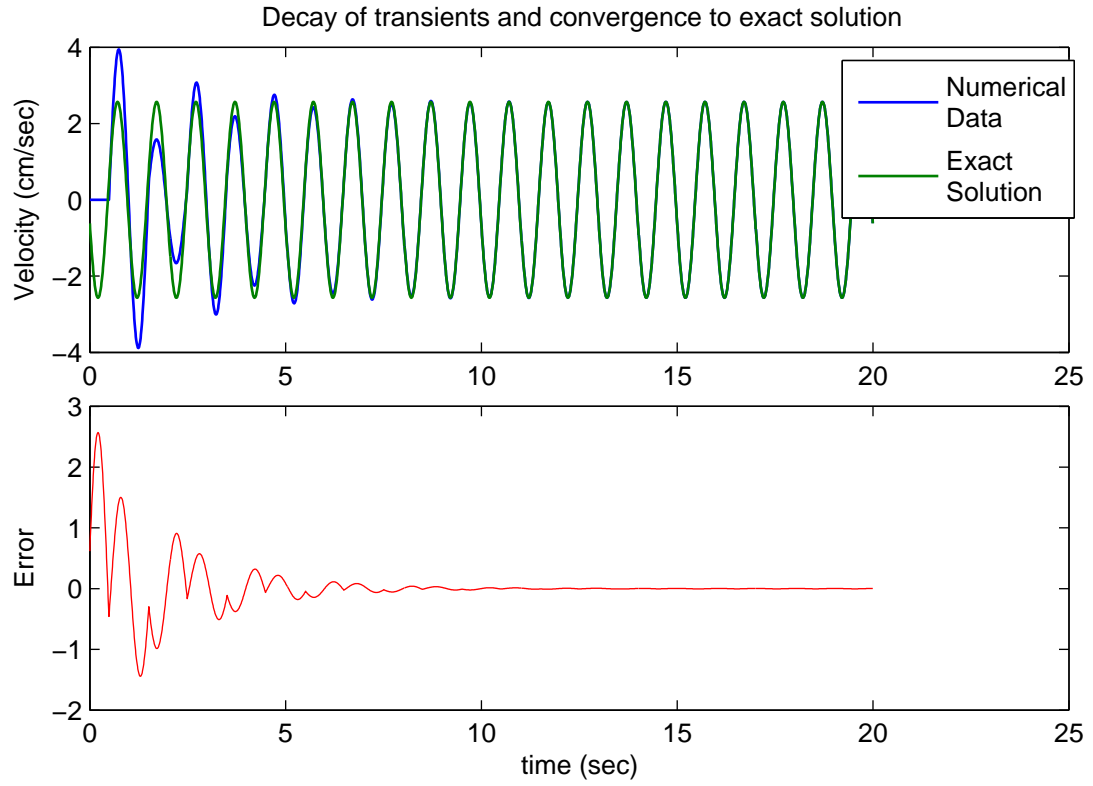
FIGURE 1.4. The numerical solution captures the onset and die-off of transient behavior as it converges to the frequency locked (exact) solution. The values used for both solutions was $\eta_0 = 100$ g/cm sec, $\lambda_0 = 1$sec, $V_0 = 5$cm/sec, $\omega = 1$Hz and $H = 10$cm.
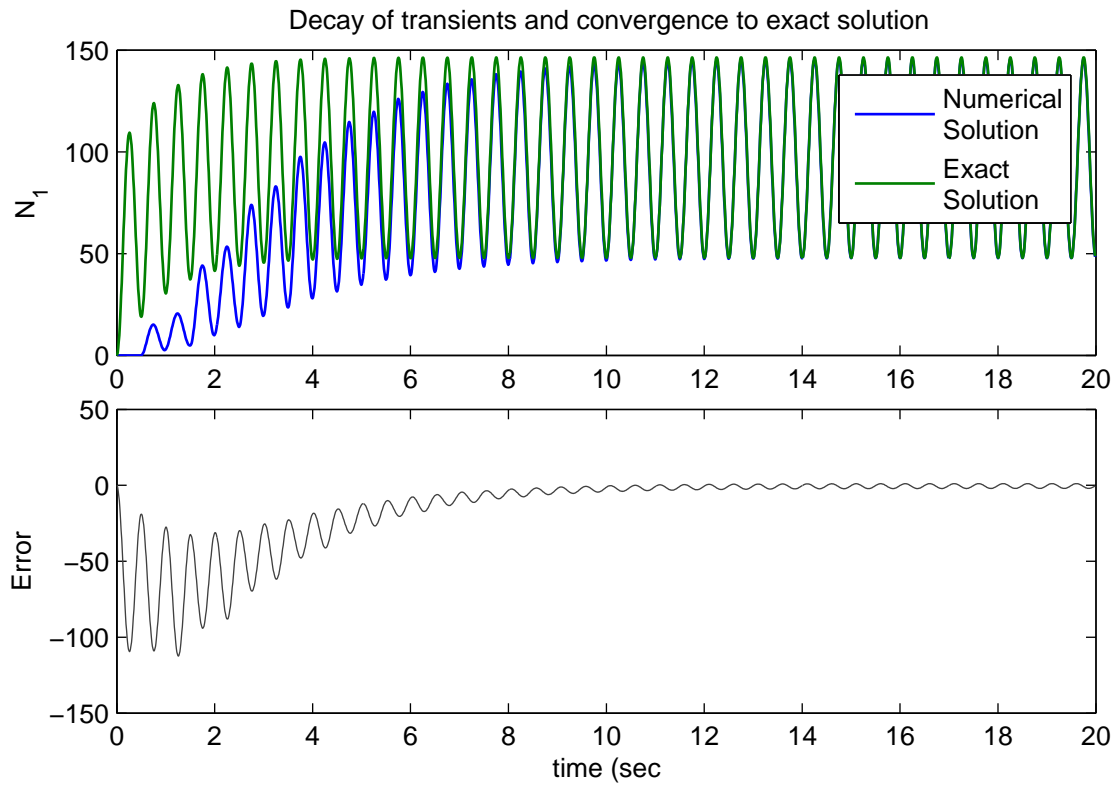
FIGURE 1.5. The numerical solution captures the onset and die-off of transient behavior as it converges to the frequency locked (exact) solution. The values used for both solutions was $\eta_0 = 100$ g/cm sec, $\lambda_0 = 1$sec, $V_0 = 5$cm/sec, $\omega = 1$Hz and $H = 10$cm.

CHAPTER 2

Experimental and modeling protocols from a micro-parallel plate rheometer

2.1. Introduction

As seen in Chapter 1, the Ferry protocol for viscoelastic characterization has several limitations. First, the channel must be deep enough, or the shear amplitude small enough so that the waves attenuate before hitting an upper interface and reflecting, distorting the signals. This means that the volume of material might have to be quite substantial in order to achieve a usable shear wave. Second, the material must exhibit strain-induced birefringence. Any fluid that doesn't exhibit this behavior cannot be characterized using the approach outlined by Ferry.

These limitations are overcome by using the generalized solution for a shear wave propagating in a parallel-plate geometry as outlined in the previous chapter, combined with the creation of a device that mimics this geometry known as the Micro-Parallel Plate Rheometer (MPPR)[1]. This device will be shown to have several advantages over the Ferry method (and other competing techniques):

- Bulk viscoelastic characterization from very small sample volumes.
- Strain controls allow for the probing of both linear and nonlinear regimes.
- Time series fitting allows for highly accurate results from a small amount of data.

---

[1]Designed by David B. Hill, Cystic Fibrosis Research Center, University of North Carolina, Chapel hill 27599-7248.

The results will show that even for sample volumes on the order of micro-liters, bulk viscoelastic parameters can be determined within acceptable error ranges when compared to another rheological device, the cone and plate rheometer.

2.2. Experimental Protocols

Device Specifications and Construction.

The MPPR is constructed by supporting a cover glass with a fixed position above a Piezo-electric stage (Mad City Labs, Madison, Wisconsin). Attached to the Piezo-electric stage is a small aluminum stage plate, to which a cover glass is attached. Two aluminum brackets, each 0.5 inches wide by 1.1 inches tall by 6.7 inches long are attached to the outer sides of the translation stage of an inverted Nikon Eclipse TE-2000 microscope. these brackets support two aluminum cross supports that hold a cover glass in place a fixed distance about the oscillating Peizo-electrical stage. The gap between the cover glasses is coarsely set through the use of known thickness shims placed between the Piezo-electric stage and a stage plate and finally with the z axis control on the Peizo stage. Figure 2.1 gives cross sectional diagrams of this device. Figure 2.2 gives a cartoon of a viscoelastic fluid entrained with 1μm beads sandwiched between the two glass slides in the MPPR. It is important to note that Figure 2.2 is not drawn to scale, as the distance between the two plates is controlled and typically chosen to be 100μm to 500μm, while the sample width is on the order of .5cm-1cm. This means there is a one to two order of magnitude difference between the height and width scales, which is important since our model will neglect the vertical boundaries at the edges of the droplet. A rough estimate of the volume of fluid in a typical experiment is given by assuming the droplet of water forms a cylinder between the two slides as drawn in Figure 2.2. Then using an estimate of 400μm for the height, and .5cm for the width of the drop gives a volume of approximately .0079cm^3 or 7.9 μl.

Data Capture.
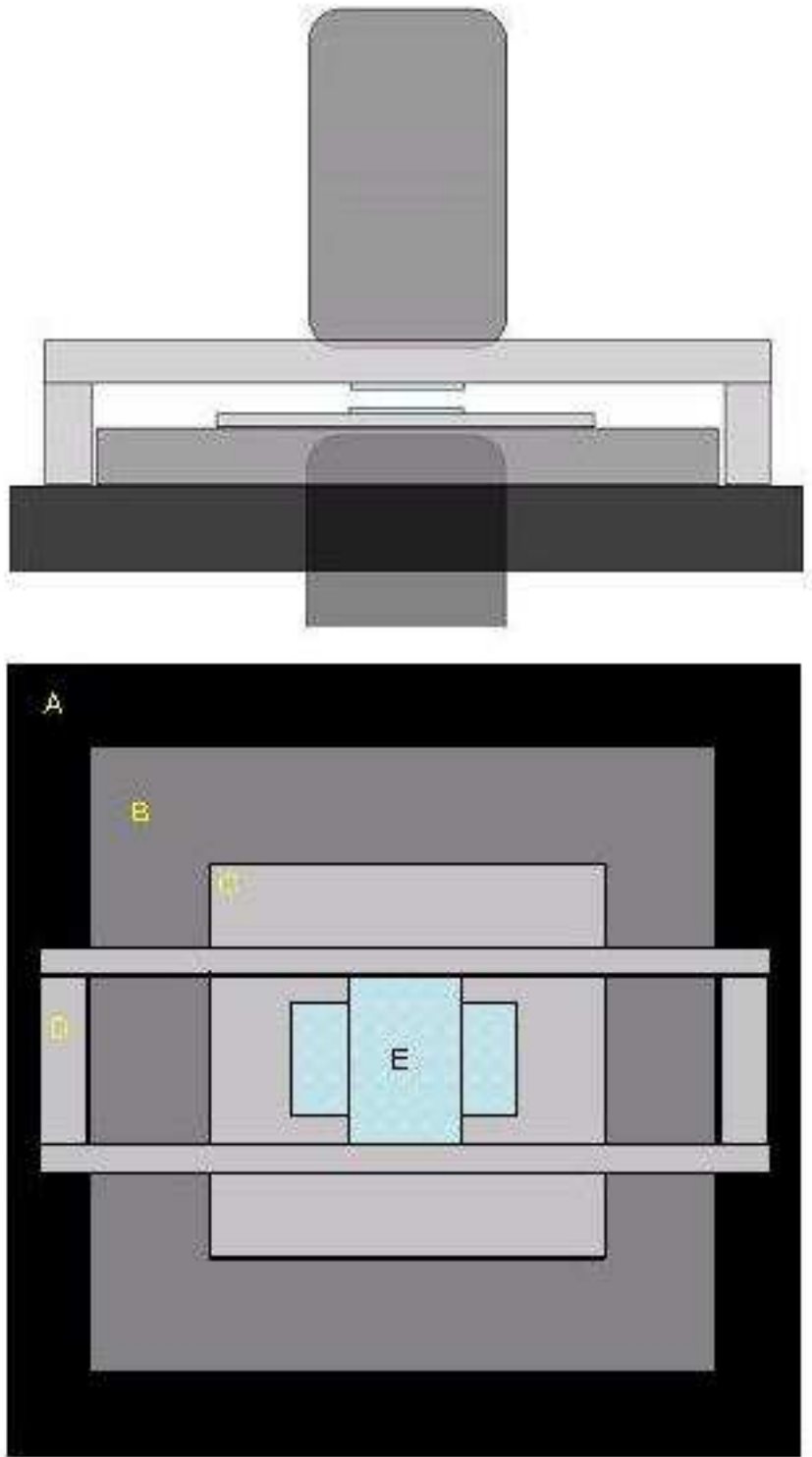
FIGURE 2.1. a) and b) Side view and top down diagrams of the MPPR. A) Microscope viewing stage. B) Stationary Piezo-electric stage base. C) Moving Piezo-electric stage D) Fixed Bracket mounts. E) Glass slide attached to bracket mounts.
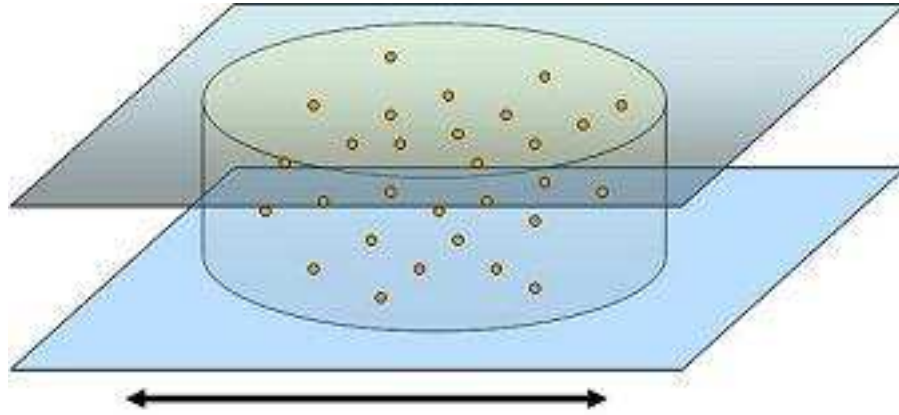
FIGURE 2.2. A side view of a fluid entrained with microbeads sandwiched between the lower moving glass slide, and the upper fixed glass slide. The length-scale of the diameter is on the order of .5-1 cm while the length-scale of the distance between the slides is $<500\mu$m.

All videos are captured at 120 frames per second (fps) using a Nikon 40x/.60 objective with a 1.5x image magnifier and a Pulnix TM-6710CL high speed digital-camera. Once collected, beads of interest within the image streams are tracked using Video Spot Tracker [2] using a symmetric tracking kernel, and the "follow jumps" option. The Video Spot Tracker takes a model based approach (based upon spherical geometry) to tracking spots, where the model of the intensity distribution within the spot is compared against an image to find the location at which the best spot is found. This position can be found to sub-pixel accuracy, and is robust to image noise that is uncorrelated with the spot cross section.

The data given by Spot Tracker is in the form of bead deformation (from the onset of tracking) in units of pixels. This data log is of the type .vrpn (for Virtual-Reality Peripheral Network) and can be converted into a Matlab readable data file using VRPN-LOGtoMatlab converter [3]. Using this file gives an easily readable comma-separated data file that Matlab or Microsoft Excel can open. The data, at this point is in terms of

---

[2]Developed by the Center for Computer Integrated Systems for Microscopy and Manipulation at UNC-Chapel Hill. Available at http://www.cs.unc.edu/Research/nano/cismm/download/spottracker/video_spot_tracker.html
[3]Also available at the above web address.

frame number and bead deformation (in units of pixels). Using a script called 'Load-VideoTracking' the units will be converted from frames into seconds and from pixels to microns (or any desired units) and the data loaded into arrays that are easily managed in Matlab. At this stage, the data is averaged over several beads (to minimize focal plane errors and noise), any linear drift subtracted (if there is non-negligible drift) and fitting to model solutions can begin.

Hyaluronic Acid Preparation.

Hyaluronic acid (HA) solutions are chosen as a test fluid for this method. These solutions were prepared from stock to a concentration of 10mg/ml in 0.2M NaCl, 0.01M EDTA with 0.01% sodium azide. The concentration was confirmed by HPLC by running 500 μL of sample on a G-25 column, attached to a Dawn EOS laser photometer coupled to a Wyatt/Optilab DSP inferometric refractometer. For experiments, 0.1% volume fraction 1.0 μm carboxilated microbeads are embedded within the fluid for the purposes of video tracking.

Cone and Plate Rheometry.

Macroscopic measurements of rheological properties of the HA solutions were made with a Bholin Gemini rheometer with a 1°, 60mm cone. Sweeps are done over a range of amplitudes to give values of η' and η'' at various strain rates. The cone and plate geometry and solutions are covered in depth in [**2, 16**], and involve measuring torque (rotational force) in response to applied rotational shear. Typically, several milliliters of fluid are needed for cone and plate measurements, versus the MPPR which can perform inverse characterization on microliters. Further, attempts to perform cone and plate rheometer measurements on ASL have resulted in catastrophic yielding of the fluid, suggesting that bulk rheological properties should be obtained at lower net strains, such as those imposed in the MPPR.

2.3. Mathematical Model

In the low strain regime, we expect a viscoelastic fluid to obey the general linear viscoelastic constitutive law. Referring to [**22**] and chapter 1 for complete solution, we summarize here the exact solution for a linear viscoelastic fluid in a shear-cell geometry. The equations of motion for a linear viscoelastic fluid are:

$$(2.1) \qquad \rho \frac{D\vec{v}}{Dt} = \nabla \cdot \boldsymbol{T} + \rho \vec{g}$$

$$(2.2) \qquad \nabla \cdot \vec{v} = 0.$$

Which give the velocity $\vec{v} = (v_x, v_y, v_z)^T$ at a time t and y units away from the lower oscillating plate. The tensor $\boldsymbol{T}$ describes the stresses in the system as a sum of the pressure contribution and the elastic contribution from the fluid, $\boldsymbol{T} = -pI + \boldsymbol{\tau}$, where $\boldsymbol{\tau}$ is the extra stress tensor which describes the elastic response of the material and is given here by the general linear viscoelastic constitutive equation,

$$(2.3) \qquad \boldsymbol{\tau} = 2 \int_{-\infty}^{t} G(t - t') \boldsymbol{D}(y, t') dt'$$

The boundary condition for driving the Peizo-electric stage is,

$$(2.4) \qquad P_x(0, t) = A \sin(\omega t),$$

where A is the amplitude of deformation in the x-axis direction and ω is frequency of oscillation in seconds times 2π. This gives a velocity boundary condition at the lower plate,

$$(2.5) \qquad v_x(0, t) = A\omega \cos(\omega t). \quad (BC1)$$

Further, the fixed slide at height $y = H$ gives the upper boundary condition,

$$(2.6) \qquad v_x(H, t) = 0. \quad (BC2)$$

We assume 1-dimensional periodic shear flow is sustained between the plates, meaning that only the v_x term of the velocity vector survives. The exact solution for the velocity profile after transients die out is then written,

$$(2.7) \qquad v_x(y,t) = Re\left(V_0 e^{i\omega t}\frac{\sinh(\delta(H-y))}{\sinh(\delta H)}\right)$$

where $V_0 = A\omega$ and the fluid parameters are carried in $\delta = \alpha + i\beta$ and are given by,

$$(2.8) \qquad \alpha = \sqrt{\frac{\rho\omega}{2|\eta^*|}\left(1 - \frac{\eta''}{|\eta^*|}\right)}$$

$$(2.9) \qquad \beta = \sqrt{\frac{\rho\omega}{2|\eta^*|}\left(1 + \frac{\eta''}{|\eta^*|}\right)}$$

For the purposes of fitting, we obtain bead path data by integrating (2.7) with respect to t and applying boundary conditions:

$$(2.10) \qquad P_x(y,t) = Re\left(\frac{V_0}{i\omega}e^{i\omega t}\frac{\sinh(\delta(H-y))}{\sinh(\delta H)}\right).$$

We now proceed by using nonlinear regression on (2.10) with respect to the viscoelastic parameters η' and η'' to fit data collected in the MPPR for HA solutions at various strain rates.

Curve Fitting and Viscoelastic analysis.

The basic algorithm for nonlinear regression involves making an initial prediction for all fitting parameters, comparing those parameters to the actual data, and making successive refinements until a desired error tolerance is reached. A summary of the method, its effectiveness, conditional convergence based upon initial guess, and other issues can be found in [1].

To begin, let $y = (y_0, y_1, ..., y_n)^T$ be experimental time history data at points $t = (t_1, t_2, ...t_n)$ and $f(t,p) = (f_0, f_1, ..., f_n)^T$ be data generated by the model solution in correspondence with the time series t, where p is the set of parameters which will be fit.

We will use a nonlinear least-squares regression to minimize the sum of the squares of the residual error, $S = r \cdot r$, with r,

$$(2.11) \qquad r = y - f(t, p).$$

This expression is minimized by taking the gradient of both sides and setting $\nabla S = 0$,

$$(2.12) \qquad A^T r = 0,$$

where A is the Jacobian matrix,

$$(2.13) \qquad A = \left(\frac{df}{dp_1}, \frac{df}{dp_2}, ..., \frac{df}{dp_n} \right).$$

Here the derivatives of f are interpreted to be nx1 vectors where each element is the derivative of f at the appropriate point in the time series. Primarily we are interested in fitting η' and η'' from the linear viscoelastic constitutive law. In this case A has dimension nx2. In general, if one is fitting m many parameters, then $dim(A) = n$xm. We now define an iterative scheme based upon successive approximation, $p^{k+1} = p^k + \Delta p$, where p^0 is an initial guess of the parameters. We can approximate the best possible choice for $f(t, p^{k+1})$ by using a first order Taylor series expanded about p^k, the current estimate,

$$(2.14) \qquad f(t, p^{k+1}) \approx f(t, p^k) + A(p^k - p^{k+1}) = f(t, p^k) + A\Delta p,$$

and solving for the Δp that minimizes the residual error at next iteration. The residual error at the next iteration is,

$$(2.15) \qquad r^{k+1} = y - f^{k+1} = y - f^k - A\Delta p = r^k - A\Delta p,$$

which is minimized by the gradient condition (2.12),

$$(2.16) \qquad A^T r^k = A^T A \Delta p,$$
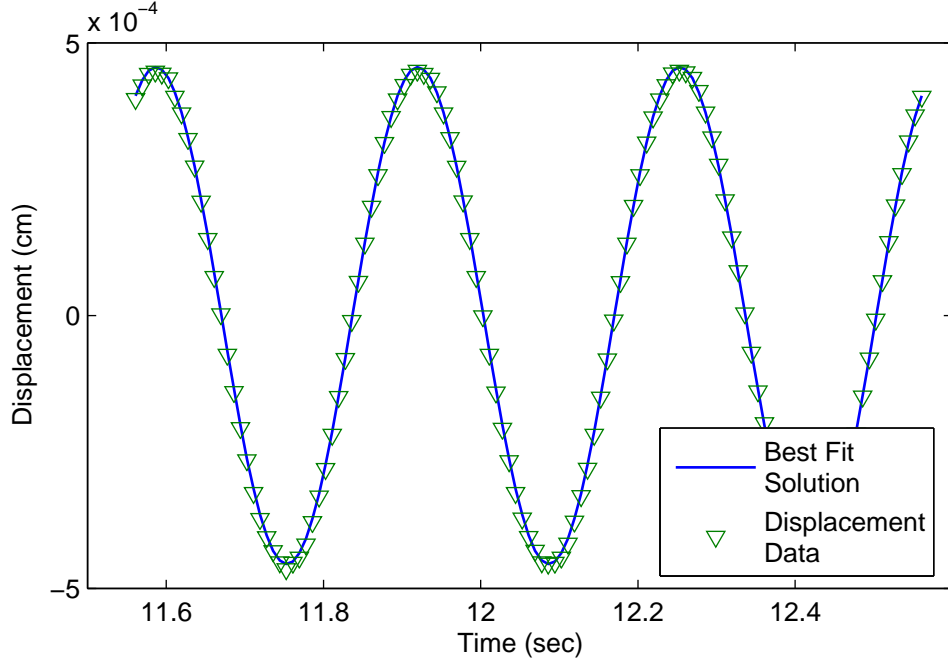
FIGURE 2.3. A typical nonlinear regression fit of the model solution to micro-bead tracking data. The experiment done here had experimental controls, $A = 5$ um, $\omega = 3$ Hz, and $H = 440$um. The bead tracked here was at 50um away from the lower plate.

which are the defining equations of the Newton-gauss Algorithm [1]. Solving for Δp gives (symbolically),

$$(2.17) \qquad \Delta p = (A^T A)^{-1} A^T r^k,$$

which gives the next step of the iterative scheme,

$$(2.18) \qquad p^{k+1} = p^k + \Delta p.$$

Typically, this scheme is run until a desired tolerance level is reached, or the algorithm runs sufficiently many times without converging to a single answer. For complicated expressions, the derivatives of f with respect to p may be computed numerically, and, in fact, this is done when fitting any of the nonlinear constitutive equations for which no exact solution exists. Figure 2.3 illustrates a typical least squares best fit of the solution for the particle displacement to data obtained by micro-bead tracking.
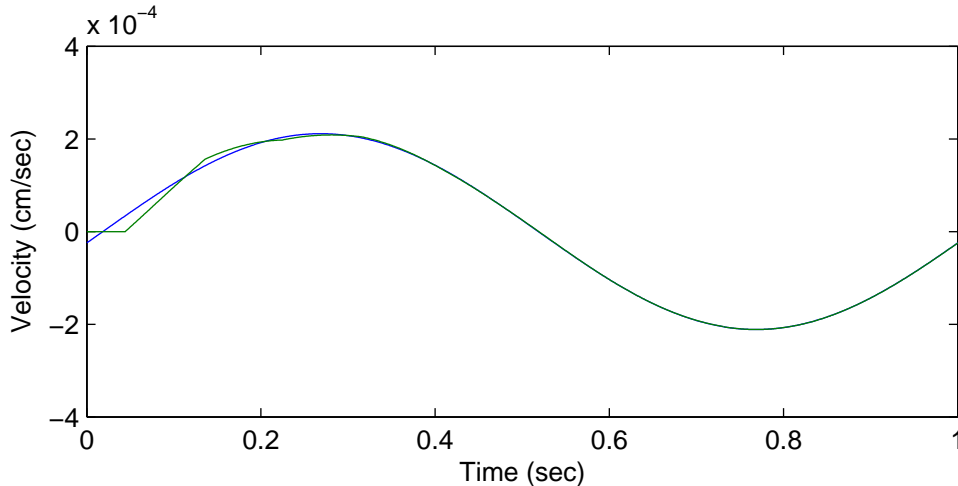
FIGURE 2.4. The decay of transients in a sample HA solution with $\eta' = 12.2$ g/cm sec and $\eta'' = 4.1$ g/cm sec and $c_0 = .4881$ cm/sec, with a channel depth of .0440 cm. The imposed lower plate velocity is 5 cm/sec at a frequency of 1 Hz.

Since the curve fitting is to the homeostatic solution, enough time must be allowed for transients to pass (as seen in Figures 1.4 and 1.5). Figure 2.4 uses test values for a hyaluronic acid sample, where η' and η'' are found experimentally in the cone and plate rheometer, to demonstrate the timescale on which transients decay. Here, $\eta' = 12.2$ g/cm sec and $\eta'' = 4.1$ g/cm sec and $c_0 = .4881$ cm/sec, with a channel depth of .0440 cm (the time series is taken at the channel midpoint). The waves are ringing across the channel more than 5 times per second, and the transients have decayed almost entirely by $t = .5$ seconds. Thus, measurements taken after half a second has elapsed should be in close agreement with the homeostatic solution.

2.4. Results

To test the accuracy and precision of the method, blind tests were carried out on a sample of HA solution using two devices: the MPPR and the cone and plate rheometer. These results, at several strain rates, are compared against the cone and plate rheometer results in Figure 2.5.
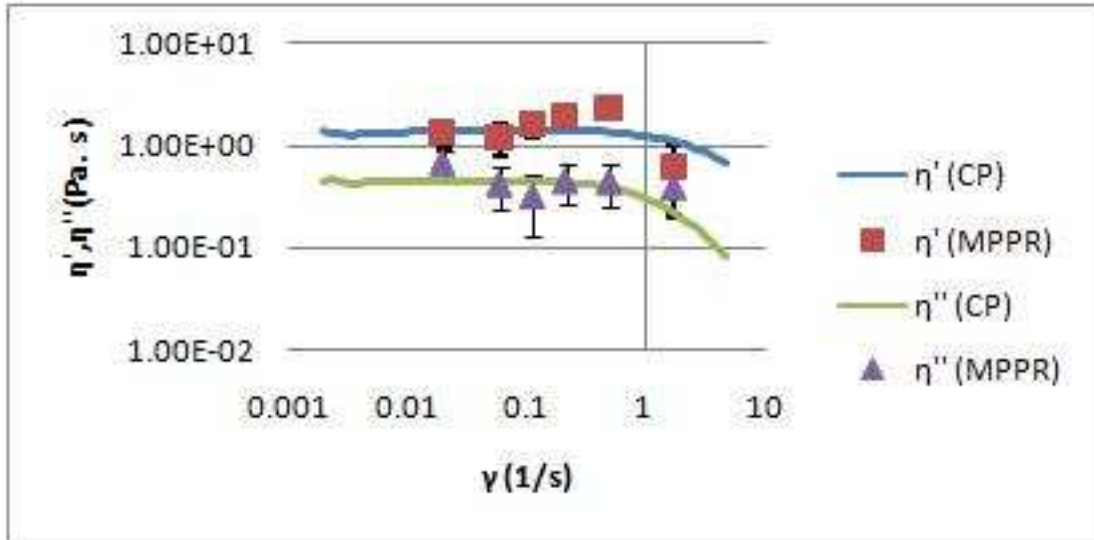
FIGURE 2.5. Graph of η' and η'' versus strain rate for the two devices, the cone and plate rheometer and MPPR.

The salient features of Figure 2.5 are that, at lower strain rates, there is very good agreement between the two measurements, with increasing error as the strain rates increase. The error bars of 2.5 are given by comparing several bead averages at different heights combined with the error ranges given by the non-linear regression code. While the agreement between conventional rheometry (cone and plate) and the MPPR values are not dead on, errors typically lie within $20 - 50\%$ between the two methods, these preliminary results are enough to warrant further study and refinement of the device and methodology, especially considering the vast improvement in terms of volume of fluid used. In fact, other micro-rheology devices, such as passive microbead diffusion, have demonstrated greater errors in predicting bulk viscoelastic properties than this method. Potential sources of error are explored just below.

2.5. Sources of Error

A fundamental assumption that allows for generation of exact solutions for this model are that the plates at $y = 0$ and $y = H$ are parallel. This allows for a one dimensional reduction of the system, satisfies the incompressibility equation, and further states that $\partial_y p = $ in the homeostatic limit. Experimentally, it is impossible to guarantee that the

plates are perfectly parallel, and the introduction of even a small deflection of the top or bottom plates renders the one-dimensional shear wave model invalid. The errors associated with a small deflection of the upper plate relative to the lower plate must be explored in a fully two-dimensional model, and the shear wave profiles of the two solutions compared to see what the effects of these errors are. As yet, no analysis has been performed on this problem. Two seemingly valid assumptions are: that the errors from a non-parallel upper plate are smaller the farther away from the upper plate you are, and that the errors are smaller in lower strain regimes. This means that, for this method, the most accurate results are likely to be obtained closer to the lower oscillating plate (typically the beads sampled at 50-100μm away from the lower plate agree with other data sources better than those farther away).

A second fundamental assumption is that the upper plate is stationary, and the lower plate is moving precisely at a controlled frequency and shear rate. The first step of fitting viscoelastic parameters using this method is to ensure the correct frequency and shear rate are obtained at the lower plate by tracking beads which are touching or are very near to the lower plate. Generally, the measured shear deformation is accurate to within 1/10th of a micron of the input shear rate. The same procedure is used to ensure the upper plate is stationary, and to determine the precise height of the upper plate (with 1-2μm). However, we know from exact and numerical simulations that normal forces are generated at the upper interface (see Chapter 3), and that they could indeed bend or flex the upper plate at precisely twice the period of the imposed shear rate. A non-stationary upper plate renders the one-dimensional assumptions invalid, and the degree of error from a flexing upper plate should be explored. Interestingly, if one could measure the time dependent force signal at the upper plate, then the stress signals could also be used as a time-series and fit to exact and numerical solutions to obtain the viscoelastic parameters.

Accuracy of measurement is always a potential source of error. The video bead tracking software tracks beads within the focal plane of the microscope, which is approximately

2 microns. Thus, the depth of the bead can be accurately measured to a particular height within a bound of $\pm 1\mu$m. To minimize this error, the height of the bead is also fit as a parameter within a boundary of $y_0 \pm .0001$ cm, where y_0 is the supposed distance of the bead from the lower plate. In the HA sample detailed above, this had a fairly minor effect on both the final values of η' and η'' as well as the error bars (the final values were within 5% of one another using both methods).

Bead drifting also provides a potential source for error. Bead drifting is assumed to be linear, and is subtracted automatically when the bead data is processed and converted into physical displacement units (typically cms). Generally, the amount of drift is very small, but at higher strain rates, drift becomes non-negligible and must be subtracted from the data before fitting to the exact solution can commence. There is no implicit reason to assume bead drift is linear however, and that it exists at higher strain rates could imply that other sources of error, such as the movement or flexing of the upper plate, or the lack of truly parallel plates, is tainting the results.

Lastly, the density, viscosity, and relaxation time of the fluid are temperature dependent values, and no attempt is made to control the temperature of the fluid beyond the ambient temperature of the room. Oscillating the lower plate at a high enough frequency could potentially raise the temperature of the fluid, but such low frequencies have been used to date (1 Hz - 6 Hz) that there is no reason to suspect that the temperature of the sample fluid is changing substantially for this reason. A larger source of heat generation is likely the microscope light, and care should be taken to ensure that the light is not raising the temperature of the media by a significant amount. To minimize the heat generated, time should be allowed between experiments for cooling of the sample to occur, and experiments should not be prolonged any longer than necessary.

2.6. Conclusion

The extension of Ferry's viscoelastic characterization protocols to finite depth via the creation of the Micro-Parallel plate rheometer, combined with modeling tools developed

above, shows promise as a new method of bulk viscoelastic characterization. The preliminary tests done so far show reproducible results that agree with current viscoelastic characterization techniques. Further refinement of the device, data capture, and fitting procedures should decrease the error ranges significantly, and further study and development is warranted. Since the curve fitting methodology doesn't implicity depend upon any particular constitutive model, even non-linear models can be fit to experimental bead deformation data, potentially allowing for non-linear viscoelastic characterization, a huge improvement over traditional methods (such as cone and plate rheometry). Future generations of this device may include an upper plate that is capable of recording normal and shear stresses. It is evident from analytical solutions in chapter 1 that normal stresses are predicted in nonlinear models, and thus normal stress signals give an indication of nonlinear behavior and could be included as data to be fit to model predictions to ascertain viscoelastic properties. A natural question then arises: what is the structure of these stress signals?

CHAPTER 3

Stress Communication and Filtering of Viscoelastic Layers in Oscillatory Strain

3.1. Introduction

The behavior of viscoelastic layers in large amplitude oscillatory shear (LAOS) has been studied in depth in the rheology literature. The methods of inquiry are varied, ranging from presumed homogeneous deformations where the problem analytically reduces to a dynamical system of ordinary differential equations [**14, 26, 25**], to presumed one-dimensional heterogeneous deformations where the models are coupled with systems of partial differential equations [**22**], to two-dimensional heterogeneity and the need for demanding numerical solver technology [**15**].

In LAOS, the rheological focus is typically on departures from linear responses and good metrics for capturing the onset and degrees of nonlinearity in the system. We refer to Giacomin et. al [**14**] and Ewoldt et. al [**6, 7**] for a scholarly treatment of the phenomenological signature of nonlinearity in LAOS. A key diagnostic for divergence from linear behavior is Lissajous figures of shear stress (τ_{xy}) versus shear rate ($\dot{\gamma}$) [**30**]. In the linear regime, the $(\dot{\gamma}(t), \tau_{xy}(t))$ Lissajous figures are characterized by thin ellipses which distort in various ways in the nonlinear regime [**14**].

The phenomenon of interest for this research is motivated by a biological query. There are countless examples in biology where a viscoelastic layer plays a vital mechanistic function. The work of Denny has studied the mechanical properties of pedal mucus and its application in gastropod locomotion [**5**]. Building on this research, Mahadevan and co-workers have developed models of mucus ratcheting as a mechanism for

gastropod transport [20], and Hosoi and co-workers have explored snail mucus and locomotion principles [8] to the point of building highly sophisticated robotic models of snail locomotion that exploit non-linear viscoelastic properties of pedal mucus to move up vertical terrains. Our focus arises from lung biology, where mucus layers line pulmonary pathways and serve as the medium between air from the external environment and the cilia-epithelium complex. The typical transport mechanism explored is mucociliary clearance, in which pathogens are trapped by mucus while coordinated cilia propel the mucus layer toward the larynx. However, another mechanical function explored by Tarran, Button, et al. [28, 29, 4] is the role of oscillatory stress in regulating biochemical release rates of epithelial cells. The role of shear stress regulating bio-chemical release rates has been studied in other contexts; for instance, it has recently been demonstrated that endothelia cilia sense fluid shear stress and play an active role in regulating chemical signaling and release rates [27, 3]. The discovery of stress-dependent biochemical release rates in epithelial cells raises fundamental questions about the stress signals arriving at the epithelial cells from a sheared mucus layer. Air-drag stresses from either tidal breathing or cough are communicated through the mucus layer to the opposing interface, whereas cilia-induced strain generates stress at the same interface. Thus, it is natural to explore one driven interface, either by time-dependent strain or stress, and then to monitor the stress or strain communication at both interfaces.

In this chapter, we impose oscillatory strain and explore interfacial stresses. This is a natural starting point for the biological application, and also happens to be the experimental configuration of finite-depth "Ferry-Stokes" viscoelastic shear waves, for which we have recently built experimental [12] and modeling [22] tools. Thus, we have ready software and analytical understanding of the coupled flow and stress waves in an oscillatory strain-driven viscoelastic layer. The studies presented here relate first to shear stress signaling, followed by the generation of normal stresses through nonlinear material properties. We focus on the upper convected nonlinearity as the common feature of all nonlinear continuum mechanical laws [16, 2]; the results remain robust in the presence

of other nonlinearities, such as the Giesekus model, where these phenomena were first discovered through numerical studies. Thus we begin the discussion with a single-mode upper convected Maxwell constitutive law, for which analysis of the authors [22] can be applied; we reveal the nature of the oscillatory dependence of stress signals with respect to all parameters.

The remainder of the chapter is organized as follows: We first recall the formulation of the model, and basic mathematical properties of the solutions relevant to oscillatory strain boundary conditions from [22]. Next, we proceed to explore stress communication. Because of nonlinearity, the analogous results with imposed oscillatory stress do not follow from the strain results: a single frequency input strain yields full harmonic stress response, and vice-versa. In the "homeostatic response", where one focuses on the frequency-locked response to the periodic strain driving condition, we can work out the precise relationship between oscillatory strain-controlled and stress-controlled experiments (section 3.4). This is true only for the upper convected Maxwell model, another argument for special attention to this simplest of all nonlinear differential constitutive laws.

We organize boundary stress signals in terms of "transfer functions" which convey specific information about the response of the viscoelastic layer. The transfer functions for this research are the extreme maximum normal and shear stress signals arriving at either plate in oscillatory strain experiments, maximized or minimized over the period of the frequency-locked response of the layer. Shear stresses oscillate with mean zero, so there is no need to track their minima. First normal stress differences of the UCM model are non-negative, so convey the bounds on normal stress generation. These transfer functions are functions of material and experimental parameters and our focus becomes the behavior with respect to each argument. One can view this strategy as an analysis of experimental parameter space. The first illustration is the behavior of the extreme boundary shear and normal stress signals for a series of experiments where the layer height is varied; we illustrate with three "model fluids" ranging from a highly elastic to

a viscoelastic to a simple viscous fluid. We show that the maximum normal and shear wall stresses exhibit strong peaks at discrete depths, with a significant drop between the peaks, except in the viscous fluid limit. For the upper convected Maxwell model, the frequency-locked response is explicitly solvable for a finite depth geometry [**22**], and thus we have explicit formulas for all wall stress transfer functions versus all parameters. The dependence on layer height happens to be the simplest to analyze and identify the nature of the peaks and valleys versus height. We then extend the results to all other parameters by numerical evaluation of the explicit formulas. Finally, to show robustness of the behavior, we shift to the Giesekus model. We generate parameter sweeps of the stress transfer functions, which now require numerical simulations of the governing system of nonlinear partial differential equations at each fixed parameter set, a parameter sweep of runs, followed by post-processing of the transfer functions. The oscillatory structure in these boundary stress signals is shown to persist; as mentioned earlier, this is indeed the context in which the phenomena were discovered, and the simplification to the UCM model was taken to gain an analytical understanding.

3.2. Mathematical Model

We recall the formulation developed in [**22**, **12**], which is a generalization of the Ferry shear wave model [**9**, **10**, **11**] to finite depth layers and nonlinear constitutive laws. We summarize the key elements from these references in order to describe the present focus on boundary stress signals in oscillatory strain experiments. The equations of motion for an incompressible fluid are,

$$(3.1) \qquad \rho \left(\frac{\partial \vec{v}}{\partial t} + (\vec{v} \cdot \nabla)\vec{v} \right) = \nabla \cdot \boldsymbol{T}$$

$$(3.2) \qquad \nabla \cdot \vec{v} = 0,$$

where $\boldsymbol{T}$ is the total stress tensor, $\vec{v}$ is the fluid velocity, and ρ is the fluid density. The total stress tensor is decomposed as $\boldsymbol{T} = -pI + \boldsymbol{\tau}$ and then the constitutive properties of the

viscoelastic material are prescribed for τ, the "extra stress tensor." We restrict attention to the simplest nonlinear constitutive law, the Upper Convective Maxwell (UCM) model, which possesses the convective nonlinearity that is common to all non-linear constitutive models. In this model, the viscoelastic properties are coarse-grained into a single elastic relaxation time (λ_0) and a single zero-shear-rate viscosity (η_0):

$$(3.3) \qquad\qquad \lambda_0 \overset{\triangledown}{\boldsymbol{\tau}} + \boldsymbol{\tau} = 2\eta_0 \boldsymbol{D},$$

where $\boldsymbol{D}$ is the rate-of-strain tensor, $\boldsymbol{D} = 1/2(\nabla\vec{v} + \nabla\vec{v}^T)$. The upper convected derivative, which makes the coupled system of flow and stress nonlinear, is defined as

$$(3.4) \qquad\qquad \overset{\triangledown}{\boldsymbol{\tau}} = \frac{\partial\boldsymbol{\tau}}{\partial t} + (\vec{v}\cdot\nabla)\boldsymbol{\tau} - \nabla\vec{v}^T\cdot\boldsymbol{\tau} - \boldsymbol{\tau}\cdot\nabla\vec{v}.$$

We assume one-dimensional shear flow in the x direction between the parallel plates and that vorticity is negligible, so that $v_y = v_z = 0$. The two parallel plates remain at heights $y = 0$ and $y = H$, with strain controls on the lower plate given by the displacement amplitude A and oscillation frequency ω. This boundary control can be stated in terms of boundary conditions on the primary velocity v_x at $y = 0$,

$$(3.5) \qquad\qquad v_x(0, t) \equiv V_0 \sin(\omega t); \quad \text{(BC1)}$$

where $V_0 = A\omega$, while the top plate is held stationary for the purposes of this problem, which sets

$$(3.6) \qquad\qquad v_x(H, t) \equiv 0. \quad \text{(BC2)}$$

The self-consistent reduction of stress yields $\tau_{xz} = \tau_{yz} = \tau_{zz} = 0$. The full model (3.1-3.4) reduces to the following closed system of partial differential equations for the remaining unknowns, $(v_x, p, \tau_{xx}, \tau_{xy}, \tau_{yy})$, which are functions of the gap height (y) and time:

$$(3.7) \qquad \rho \frac{\partial v_x}{\partial t} = \frac{\partial \tau_{xy}}{\partial y}$$

$$(3.8) \qquad \frac{\partial p_y}{\partial y} = \frac{\partial \tau_{yy}}{\partial y}$$

$$(3.9) \qquad \lambda_0 \frac{\partial \tau_{xx}}{\partial t} - 2\lambda_0 \frac{\partial v_x}{\partial y} \tau_{xy} + \tau_{xx} = 0$$

$$(3.10) \qquad \lambda_0 \frac{\partial \tau_{xy}}{\partial t} - \lambda_0 \frac{\partial v_x}{\partial y} \tau_{yy} + \tau_{xy} = \eta_0 \frac{\partial v_x}{\partial y}$$

$$(3.11) \qquad \lambda_0 \frac{\partial \tau_{yy}}{\partial t} + \tau_{yy} = 0.$$

We are only concerned with "homeostatic" responses for this study, in particular the frequency-locked response of the fluid layer to the boundary control. Thus we suppress the effects of transients and initial conditions on velocity, pressure and stress. From (3.11), τ_{yy} decays exponentially to zero, and from (3.8) any pressure gradient likewise converges rapidly to zero. In [22], a complete solution of this problem is derived resting on the observation that v_x and τ_{xy} decouple into a linear hyperbolic system once τ_{yy} is negligible, and then the remnant of nonlinearity from the upper convective derivative reduces to the solution of (3.9) with known functions for the velocity and shear stress. The 2x2 system (3.7, 3.9, satisfying BC1 and BC2) is solved, in the $H = \infty$ limit by Ferry et al. [9, 10, 11], and generalized to any finite H by the authors [22]:

$$(3.12) \qquad v_x(y,t) = \mathcal{I}m\left(V_0 e^{i\omega t} \frac{\sinh(\delta(H-y))}{\sinh(\delta H)}\right)$$

$$(3.13) \qquad \tau_{xy} = \mathcal{I}m\left(-V_0 \eta^* \delta \; e^{i\omega t} \frac{\cosh(\delta(H-y))}{\sinh(\delta H)}\right).$$

Here we have introduced the complex viscosity, $\eta^* = \eta' - i\eta''$ which, for a single-mode Maxwell fluid is,

$$(3.14) \qquad \eta' = \frac{\eta_0}{1 + (\omega\lambda_0)^2}$$

$$(3.15) \qquad \eta'' = \frac{\eta_0\omega\lambda_0}{1 + (\omega\lambda_0)^2}.$$

The key complex parameter in the response functions for v_x and τ_{xy} is

$$(3.16) \qquad \delta = \alpha + i\beta,$$

the same notation and parameter identified by Ferry in the semi-infinite layer limit, which is given for the single mode Maxwell model by:

$$(3.17) \qquad \alpha = \sqrt{\frac{\rho\omega}{2\eta_0}\left(\sqrt{1 + \omega^2\lambda_0^2} - \omega\lambda_0\right)}$$

$$(3.18) \qquad \beta = \sqrt{\frac{\rho\omega}{2\eta_0}\left(\sqrt{1 + \omega^2\lambda_0^2} + \omega\lambda_0\right)}.$$

This solution, though written here for the UCM model, is a special case of the solution for a general linear viscoelastic fluid [22, 9]. The real parameters α and β correspond physically to the attenuation length and wavelength described by Ferry in the semi-infinite domain problem. In the finite depth layer, our formulas resolve counter-propagating waves and thus the physical significance of α and β is not transparent in a snapshot; instead we have developed inverse characterization protocols based on microbead tracking and single particle paths [12].

We proceed now to the focus of this discussion, namely stress boundary signals. With the exact expressions for v_x and τ_{xy}, the evolution of τ_{xx} is now explicitly given by a

quadrature solution of (3.9), where initially τ_{xx} is assumed to be zero:

$$(3.19) \qquad \tau_{xx}(y,t) = 2 \int_0^t e^{(t'-t)/\lambda_0} \frac{\partial v_x}{\partial y}(y,t')\tau_{xy}(y,t')dt'.$$

The convolution integral cannot be carried out explicitly (at least not under the weight of our pen thus far), but can be numerically evaluated. The transfer functions of interest are then given for the UCM model by evaluation of these formulas at $y = 0$ or $y = H$. Note that since $\tau_{yy} = 0$ in the UCM model after transients have passed, the first normal stress difference $N_1 = \tau_{xx} - \tau_{yy}$ and τ_{xx} are used interchangeably until we get to the Giesekus model simulations.

3.3. Stress Selection Criteria

The primary focus of most studies of large amplitude oscillatory shear (LAOS) is on the dynamic (time-dependent) responses in a given experiment. The dynamic response functions sometimes presume homogeneous deformations [14] while other studies explore heterogeneity [15]. Our study admits 1-dimensional heterogeneity, but we are interested in stress information arriving at layer boundaries. For a given realization of the experiment, we extract the extreme boundary shear and normal stress signals arriving at either the driven interface or the opposing stationary interface. The wall shear stress oscillates with mean zero and the maximum and minimum values have the same magnitude, so only the maximum of shear stress is reported. The normal stress τ_{xx} is non-negative, so both extreme values are reported to convey the range of normal stress generation. These "transfer functions" are denoted: $\max_t \tau_{xy}(0,t)$, $\max_t \tau_{xy}(H,t)$, $\max_t \tau_{xx}(0,t)$, $\min_t \tau_{xx}(0,t)$, $\max_t \tau_{xx}(H,t)$, and $\min_t \tau_{xx}(H,t)$. To begin the discussion we consider $\max_t \tau_{xy}(0,t)$. Later, after we identify salient features of these transfer functions, we return to the more traditional Lissajous figures of the time-dependent stress and shear rate, and illustrate their variation with model control parameters.

Analysis of Interfacial Stress Signals.

Consider the following "layer" transfer function: the maximum shear stress of the frequency-locked response, maximized over time, retaining its dependence on gap height:

$$(3.20) \qquad \max_t \tau_{xy}(y,t) = \max_t \mathcal{I}m\left(-\delta V_0 \eta^* e^{i\omega t} \frac{\cosh(\delta(H-y))}{\sinh(\delta H)}\right).$$

For any fixed gap height, the maximum stress response reduces to analysis of this function as a function of the material and experimental parameters. At the lower plate, the shear stress response function is easily derived (by finding the time of maximum stress over each period $2\pi/\omega$ and then evaluating at that time):

$$(3.21) \qquad \tau_{xy}^{max}(\rho, \lambda_0, \eta_0, \omega, H) = V_0 |\delta| \|\eta^*\| |\coth(\delta H)|.$$

Height-dependent oscillatory structure in shear stress signals.

The simplest dependence of $\tau_{xy}^{max}(\rho, \lambda_0, \eta_0, \omega, H)$, equation (3.21), is with respect to H, the layer height, for which the dependence is proportional to $|\coth(\delta H)|$. Thus, the H-dependence reduces to a real-valued function of a complex argument, δH, where δ is the complex quantity defined in equations (3.16)-(3.18). For fixed material properties ρ, η_0 and λ_0, and driving frequency ω, the dependence on H reduces to the evaluation of $|\coth(\delta H)|$ along the ray δH in the complex plane. Figure 3.1 provides a graph of the complex values of $\coth(\delta H)$ for a range of H in three physically distinct model fluids: a strongly elastic fluid with $\eta_0 = 1000$ g/cm sec and $\lambda_0 = 10$sec, a viscoelastic fluid with $\eta_0 = 100$ g/cm sec and $\lambda_0 = 1$sec, and a viscous fluid with $\eta_0 = 1$ g/cm sec and $\lambda_0 = 0$sec. The spiral nature of the $\coth(\delta H)$ function simply reflects the exponential behavior for real δ and the oscillatory behavior for imaginary δ. Clearly the polar angle of the complex number δ (i.e. the ray δH) determines whether the stress signals are dominated by exponential or oscillatory behavior of the coth function. This is made precise just below.

Figure 3.2 plots the transfer function $\tau_{xy}^{max}(\rho, \lambda_0, \eta_0, \omega, H)$, which is proportional to the modulus of the complex-valued spiral in Figure 1, for the same three model fluids.
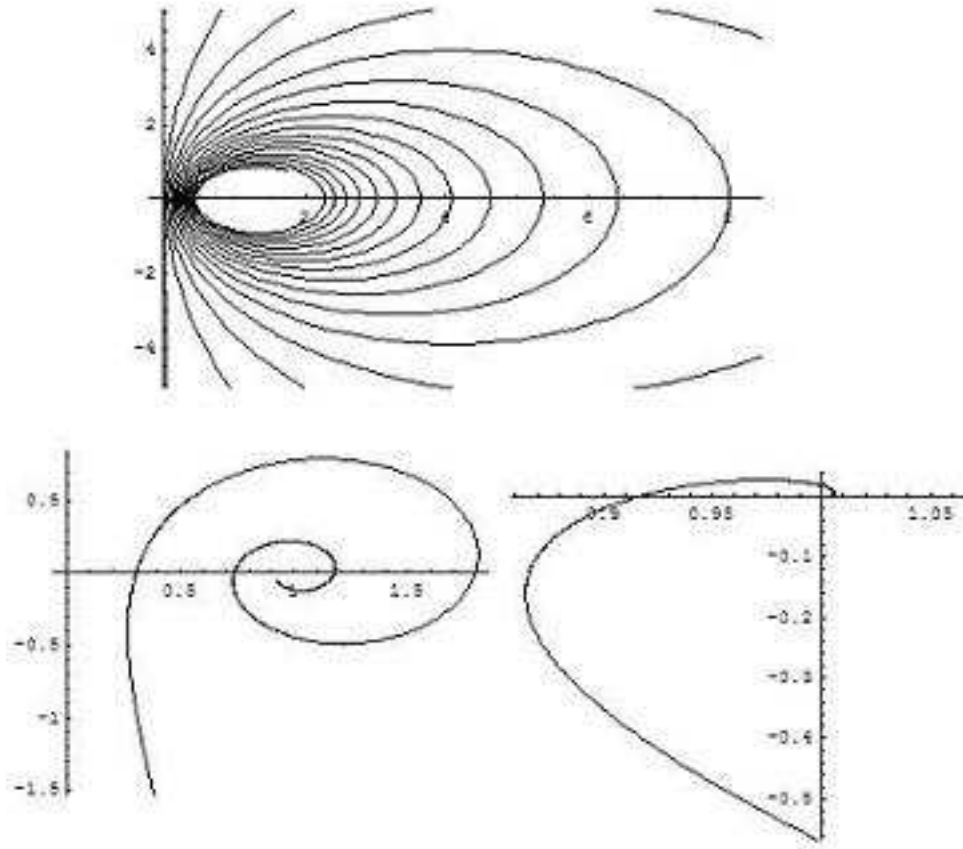
FIGURE 3.1. Evaluation of $\coth(\delta H)$ as a complex-valued function over a range $[H_{min}, H_{max}]$ for three model fluids: counter-clockwise from the top, a highly elastic fluid with Maxwell parameters $\eta_0 = 1000$ g/cm sec, $\lambda_0 = 10$sec, a viscoelastic fluid with $\eta_0 = 100$ g/cm sec, $\lambda_0 = 1$sec, and a fluid near the viscous limit with $\eta_0 = 1$ g/cm sec, $\lambda_0 = .01$sec. Henceforth, we refer to these parameter choices as Model Fluid 1, 2 and 3. For future reference, we note that $\alpha/\beta = .0080$ for Model Fluid 1, $\alpha/\beta = .0791$ for Model Fluid 2 and $\alpha/\beta = .9391$ for Model Fluid 3.

Clearly, there are oscillations versus layer height in the shear stress signal at the driven plate (in the highly elastic and viscoelastic regimes), with envelopes of the successive peaks and valleys that derive from the exact formula. The peaks and valleys of Figure 3.2 correspond to the apogee and perigee of Figure 3.1, respectively.

The apparent regularity of the locations of the peaks and valleys in the maximum plate stress signal versus H is dependent on the fluid parameters and frequency chosen in Figure 3.1. Note, as we approach the viscous limit, the peaks and valleys vanish. If
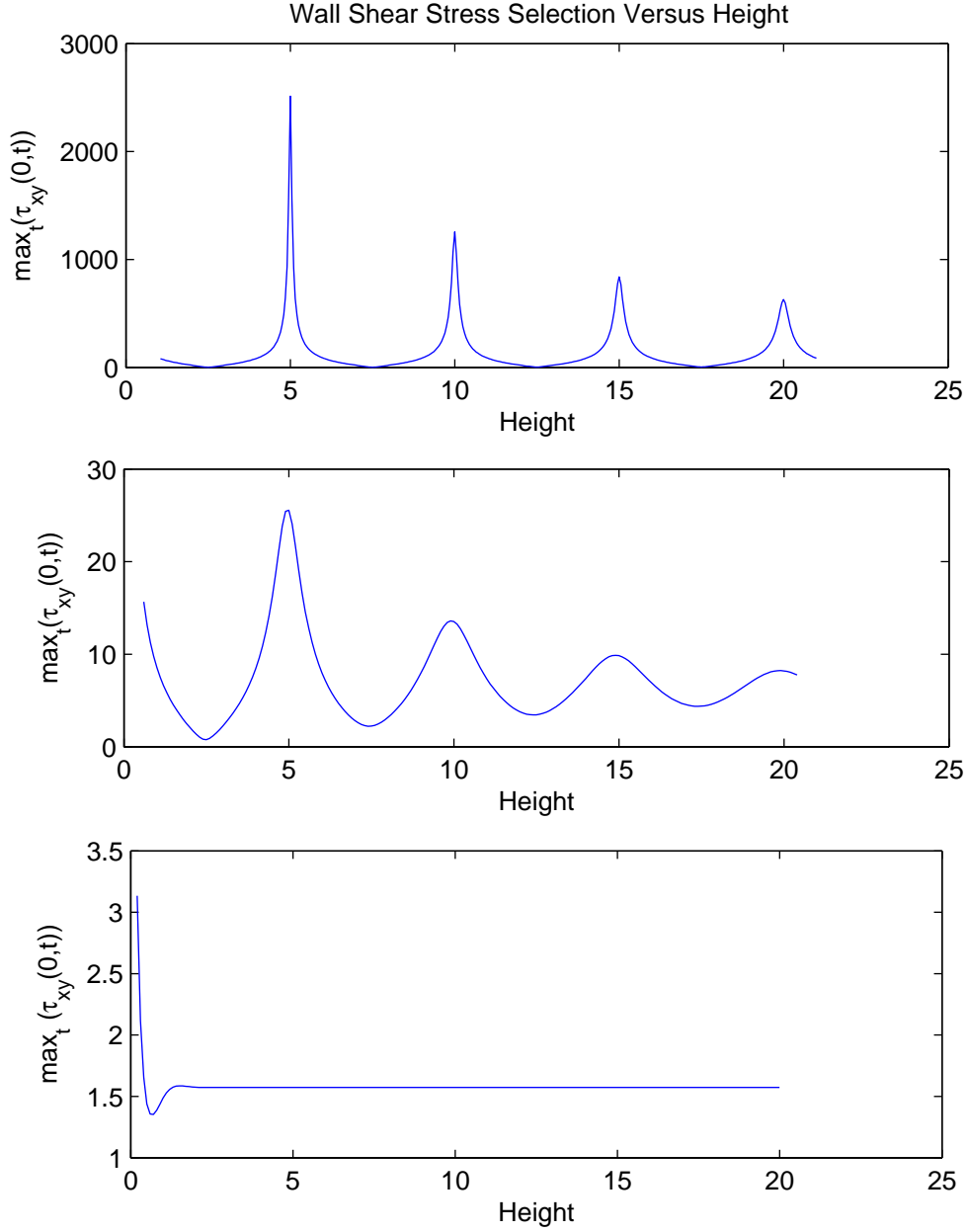
FIGURE 3.2. Maximum shear stress at the lower plate versus layer depth (equation 21) for the three model fluids. The peaks and valleys of the response function correspond to the apogee and perigee, respectively, of the spirals in Fig 1. For these runs the driving conditions are $A = .1$cm and $\omega = 1$Hz.

we express $|\coth(\delta H)|$ as follows,

$$(3.22) \qquad |\coth(\delta H)|^2 = \frac{\sin^2(2\beta H) + \sinh^2(2\alpha H)}{(\cos(2\beta H) - \cosh(2\alpha H))^2},$$

the dual periodic and exponential dependence is transparent. If the material parameters yield α small with respect to β, for instance a model fluid with $\eta_0 \approx 100\mathrm{cmg/s}$ with a relaxation time of approximately 1s, which renders α smaller than β by an order of magnitude, then the peaks are very regularly spaced. In a viscous fluid, such as Model Fluid 3 in Figures 3.1 and 3.2, $\alpha = \beta$ and the oscillatory structure vanishes.

From (3.19), we also have a closed-form expression for the first normal stress difference $N_1 = \tau_{xx}$ (since $\tau_{yy} = 0$). Fig 3.3 is a plot of τ_{xx}^{max} and τ_{xx}^{min} at $y = 0$, again for a range of layer depths. Note that the maxima and minima occur at the same values of H as the maximum shear stress. This property will be illustrated in more depth below.
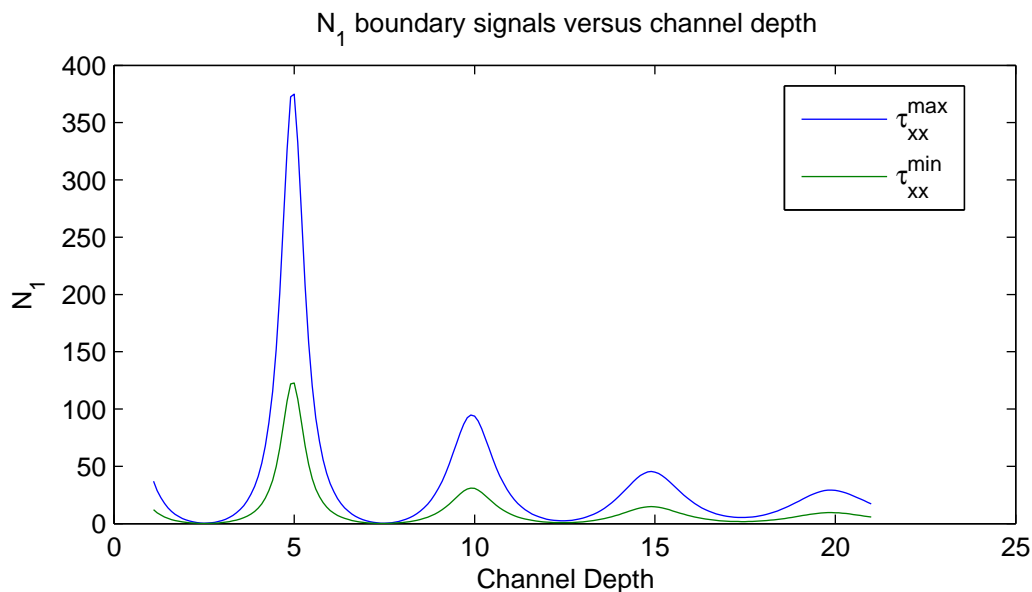
FIGURE 3.3. Maximum and minimum first normal stress difference N_1 at the lower plate versus layer depth (equation 21) for Model Fluid 2 of Figures 1 and 2 (note $\tau_{yy} = 0$ after transients have passed).

3.4. Lissajous Figures

Imposed Shear Rate and Implied Shear Stress.

As suggested by Tee and Dealy [30], shear stress or normal stress versus shear rate loops represent the most useful manner of studying the behavior of viscoelastic fluids in oscillatory shear. These figures are simply parametric plots of the time varying stress

relative to the local shear rate, in our model denoted as τ_{xy} or τ_{xx} and $\dot{\gamma}$ respectively. In the simplest case of a linear viscoelastic fluid undergoing a known periodic shear of frequency (ω) where the periodic shear rate is defined by,

$$\dot{\gamma}(t) = \gamma_0 \omega \cos(\omega t),$$

the shear stress versus shear rate loop is known to be an ellipse [14], and is defined by the equation :

(3.23) $\qquad (\tau_{xy}^0)^2 \dot{\gamma}^2 - 2\tau_{xy}^0 \gamma_0 \omega \sin(\phi) \tau_{xy} \dot{\gamma} + \gamma_0^2 \omega^2 \tau_{xy}^2 - (\tau_{xy}^0)^2 \gamma_0^2 \omega^2 \cos^2(\phi) = 0.$

To understand this formulation, we refer to the reduced equation describing the evolution of shear stress. Recall that, for uniformly periodic shear stress in the x-axis direction,

(3.24) $\qquad \lambda_0 \dfrac{\partial \tau_{xy}}{\partial t} - \lambda_0 \dfrac{\partial v_x}{\partial y} \tau_{yy} + \tau_{xy} = \eta_0 \dfrac{\partial v_x}{\partial y}$

Recalling that the shear rate is, by definition, the gradient of the velocity in a flowing material,

(3.25) $\qquad \dot{\gamma} = \dfrac{\partial v_x}{\partial y} + \dfrac{\partial v_y}{\partial x}$

and that τ_{yy} decays to zero in the long-time limit [22], we arrive at an ODE in τ_{xy}

(3.26) $\qquad \lambda_0 \dfrac{\partial \tau_{xy}}{\partial t} + \tau_{xy} = \eta_0 \dot{\gamma}(t)$

Where the initial value of $\tau_{xy}(0) \equiv 0$. It is a straightforward exercise in integration by parts, as shown below, to get the solution of this equation, also given in [22] and [14]. Using the variation of parameters method on (3.24) gives,

(3.27) $\qquad \dfrac{d}{dt}(e^{t/\lambda_0} \tau_{xy}) = G_0 e^{t/\lambda_0} \gamma_0 \omega \cos(\omega t).$

Integration by parts twice on the right hand side gives,

$$(3.28) \qquad e^{t/\lambda_0}\tau_{xy} = \gamma_0 \frac{G_0\lambda_0\omega}{1+(\lambda_0\omega)^2}e^{t/\lambda_0}(\cos(\omega t) + \lambda_0\omega \sin(\omega t)) + C.$$

From here, we define τ_{xy}^0 as,

$$(3.29) \qquad \tau_{xy}^0 = \gamma_0 \frac{G_0\lambda_0\omega}{1+(\lambda_0\omega)^2},$$

and rewrite,

$$(3.30) \qquad \tau_{xy} = \tau_{xy}^0(\cos(\omega t) + \lambda_0\omega \sin(\omega t)) + e^{-t/\lambda_0}C.$$

and recognize that if we restrict our attention to the phase locked solution (i.e. long time limit) then the choice of integration constant C becomes irrelevant. Indeed, we can choose $C = 0$ to examine the phase locked solution. Now, introducing the phase shift angle ϕ such that $\sin\phi = 1$ and $\cos\phi = \omega\lambda_0$ or,

$$(3.31) \qquad \phi = \arctan\frac{1}{\lambda_0\omega},$$

and employing the formula for the addition of angles on sine gives,

$$(3.32) \qquad \tau_{xy}(t) = \tau_{xy}^0 \sin(\omega t + \phi).$$

This is certainly not the only formulation for the shear stress for a given shear rate. An alternate, but equivalent, formulation is given in the following subsection. The equation for the ellipse (3.23) is found by considering the parametric equations defining the shear stress and the shear rate,

$$(3.33) \qquad \dot{\gamma}(t) = \gamma_0\omega \cos(\omega t)$$

$$(3.34) \qquad \tau_{xy}(t) = \tau_{xy}^0 \sin(\omega t + \phi),$$

over some time domain $[t_{min}, t_{max}]$. We invert equation (3.33) and solve for t,

$$(3.35) \qquad t = \frac{1}{\omega} \cos^{-1}\left(\frac{\dot{\gamma}}{\gamma_0 \omega}\right).$$

Using this definition of t, and plugging into equation (3.34) and applying the addition of angles formula for sine, we get,

$$(3.36) \qquad \tau_{xy} = \tau_{xy}^0 \left(\frac{\dot{\gamma}}{\gamma_0 \omega} \sin(\phi) + \frac{\sqrt{\gamma_0^2 - \dot{\gamma}^2}}{\gamma_0 \omega} \cos(\phi) \right).$$

Finally, some simplification and squaring both sides of the equation gives precisely the result of equation (3.23), which is the same result given by Giacomin [14].

Alternative Formulation.

Now, recalling the definition of the complex modulus for a single mode Maxwell fluid,

$$(3.37) \qquad G^* = G' + iG'',$$

where,

$$(3.38) \qquad G' = \frac{G_0(\lambda_0 \omega)^2}{1 + (\omega\lambda_0)^2}$$

$$(3.39) \qquad G'' = \frac{G_0 \lambda_0 \omega}{1 + (\omega\lambda_0)^2}$$

and we rewrite equation (3.28) as,

$$(3.40) \qquad \tau_{xy} = \gamma_0(G'' \cos(\omega t) + G' \sin(\omega t)) + e^{-t/\lambda_0} C.$$

In this form we can clearly see the emergence of the in phase and out of phase components of the shear stress. In order to make the parametric formulation more clear, consider the substitutions $\sin(\psi) = G''$ and $\cos(\psi) = G'$, or equivalently,

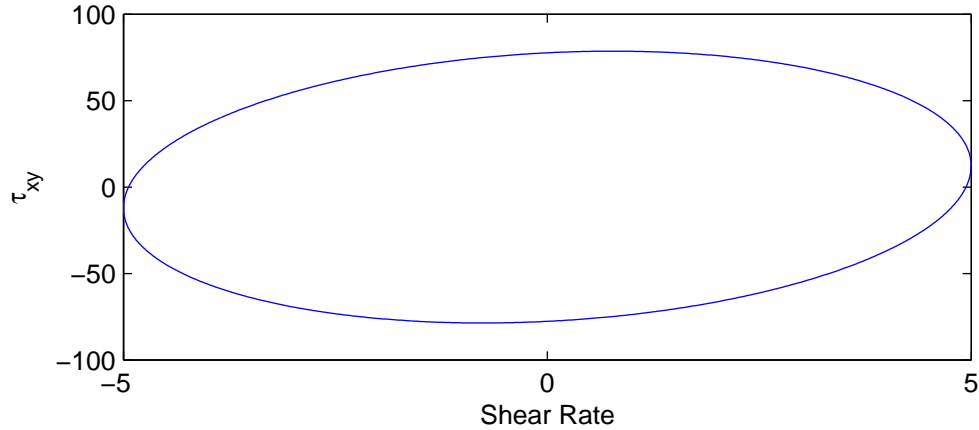$$(3.41) \qquad \psi = \arctan\left(\frac{G''}{G'}\right).$$

FIGURE 3.4. Lissajous figure for Model fluid 2 for local imposed maximum shear rate of 5 sec^{-1}.

Then, after applying the addition of angles formula for sine, equation (3.40) becomes,

$$(3.42) \qquad \tau_{xy} = \gamma_0 \sin(\omega t + \psi).$$

This form can be substituted for equation (3.34), and an alternate (but equivalent) form of the ellipse given [**14**]. The ellipse for Model fluid 2 is given below.

The Semi-Infinite Domain Problem.

Rather than imposing the shear rate $\dot{\gamma}$ at a particular point within the fluid, we consider the half-plane geometry of Ferry where an oscillatory shear is imposed at $y = 0$ with known amplitude A and frequency ω. Here,

$$(3.43) \qquad v_x(t, 0) = A\omega \sin(\omega t)$$

along with the constraint

$$(3.44) \qquad \lim_{y \to \infty} v_x(y, t) = 0$$

Has the exact solution,

$$(3.45) \qquad v_x(t, y) = A\omega e^{-\alpha y} \sin(\omega t - \beta y),$$

which means that the local shear rate at any height y is given by,

$$(3.46) \qquad \dot{\gamma}(t, y) = -A\omega e^{-\alpha y}(\alpha \sin(\omega t - \beta y) + \beta \cos(\omega t - \beta y)).$$

Introducing the substitution $\alpha = \sin(\psi)$ and $\beta = \cos(\psi)$ or equivalently, $\psi = \arctan(\alpha/\beta)$ and using the addition of angles formula on cosine gives,

$$(3.47) \qquad \dot{\gamma}(t, y) = -A\omega e^{-\alpha y} \cos(\omega t - \beta y - \psi),$$

which is a variation of equation (3.23) that includes a phase lag factor for the shear rate at any point y as a function for how far that point is from the moving (bottom) plate. The exact solution for the shear stress is given by [22] and in Chapter 1,

$$(3.48) \qquad \tau_{xy}(t) = \tau_{xy}^0(y) \sin(\omega t - \beta y + \phi),$$

where the phase shift of the tangential stress with respect to the velocity is,

$$(3.49) \qquad \phi = \arctan(\beta/\alpha) + \pi,$$

and where α and β are given by Ferry's exact solution [10] and cited here in Chapter 1. The pre-factor for the shear stress is given by,

$$(3.50) \qquad \tau_{xy}^0 = \frac{\gamma_0 \omega}{\beta^2 - \gamma_0 \omega^2 \alpha^2} e^{-\alpha y}.$$

For comparison with the results in the previous section, we offset time by an appropriate factor,

$$(3.51) \qquad t = t' + 1/\omega(\beta y + \psi)$$

And write the parametric equations with respect to this frame,

$$(3.52) \qquad \dot{\gamma}(t') = \gamma_0 \omega \cos(\omega t')$$

$$(3.53) \qquad \tau_{xy}(t') = \tau_{xy}^0 \sin(\omega t' + \tilde{\phi}),$$

where $\tilde{\phi} = \psi + \phi$. We now have a parametric formulation for every height y that is equivalent (up to choice of time frame) to the formulation above. Now, using the exact same algebra, we get the equation for the ellipse,

$$(3.54) \qquad (\tau_{xy}^0)^2 \dot{\gamma}^2 - 2\tau_{xy}^0 \gamma_0 \omega \sin(\tilde{\phi}) \tau_{xy} \dot{\gamma} + \gamma_0^2 \omega^2 \tau_{xy}^2 - (\tau_{xy}^0)^2 \gamma_0^2 \omega^2 \cos^2(\tilde{\phi}) = 0.$$

which is the same as that given by Giacomin [14]. We now analyze the properties of Lissajous figures in the finite depth problem, and explore the effect of layer depth on these figures.

The finite depth problem.

Following the work of Keunings et. al and Giacomin et. al [15, 14], Figure 3.4 presents Lissajous figures which show the dynamics of shear stress versus shear rate for a given model experiment (here with a fixed upper interface at height $y = H$). For this sweep, we present only the Lissajous figures for Model Fluid 2, but recognize that Model Fluid 1 will exaggerate the results of Figure 3.2, while Model Fluid 3 suppresses the phenomenon entirely. For linear viscoelastic fluids in a semi-infinite domain, the Lissajous figure is a slanted, thin ellipse where the slant angle is determined by the ratio β/α of the real and complex parts of δ [14], and is given as $\phi = \tan^{-1} \alpha/\beta$. In the viscous fluid limit, where $\alpha = \beta$, the slant angle of the ellipse is precisely 45 degrees. Fig. 3.4, also shows the extreme values of shear stress at these heights for Model Fluid 2 which are 3 of the data points in Figure 3.3.

Next, in Figure 3.5 we give the analogous Lissajous figures of the normal stress τ_{xx} versus shear rate, for the same simulations of Figure 3.4. The key features are: the normal stress has half the period of the shear stress and shear rate, and the extreme values are clearly non-monotone versus layer height H. Lastly, in Figure 3.6, we present Lissajous figures of the first normal stress difference N_1 versus the shear stress τ_{xy}. We find non-monotone behavior consistent with previous Figures, but further, oscillations in the relative extreme values of N_1 and τ_{xy}. Thus, changing the height of the layer also
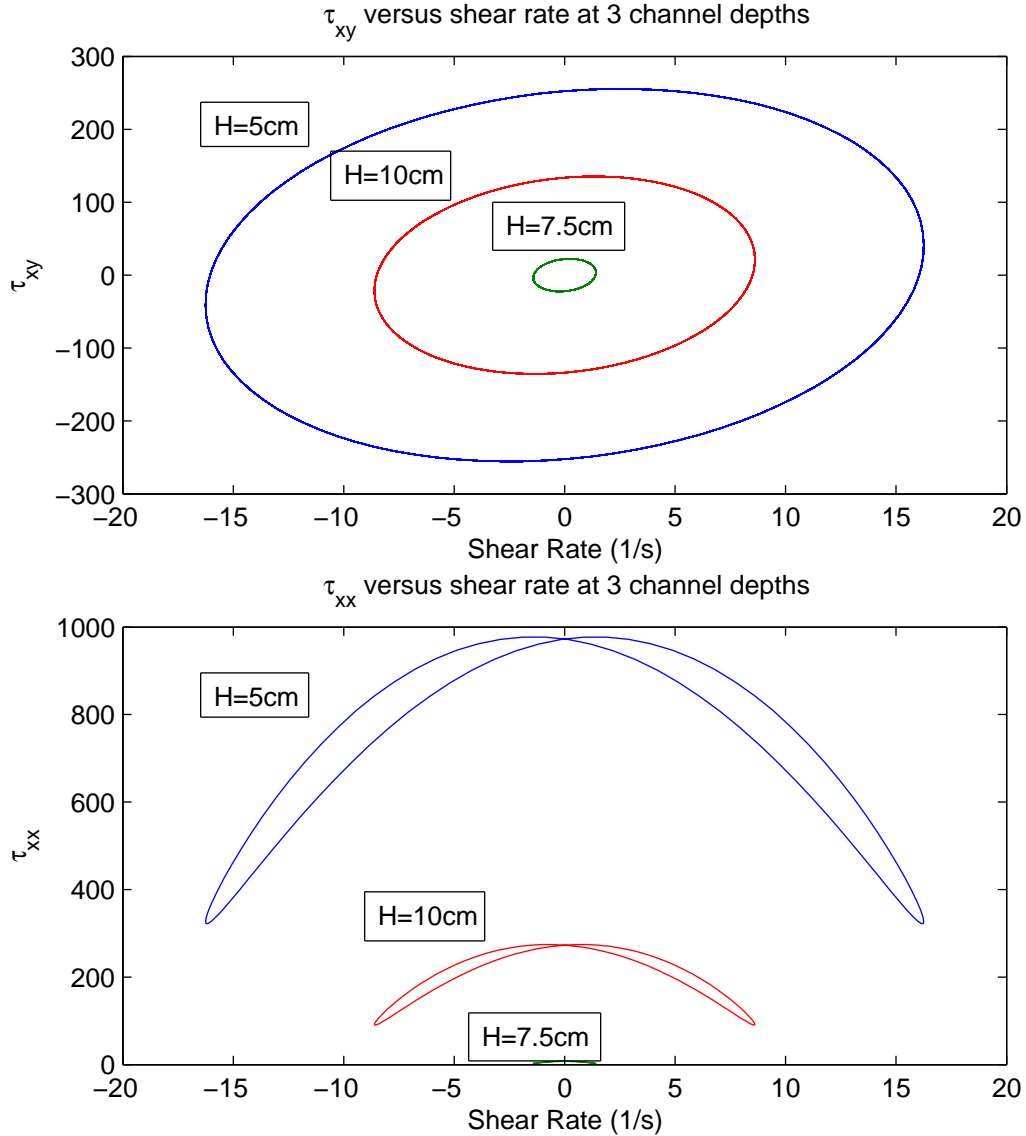
FIGURE 3.5. Lissajous figures of shear and normal stress vs. shear rate of Model Fluid 2 for three distinct layer heights, H=5,7.5,10cm, with a driving frequency of 1Hz and lower plate displacement of .1cm. a) Shear stress versus shear rate. b) Normal stress versus shear rate.

controls the relative magnitude of the stress components. It is also clear that the maxima and minima of the shear and normal stresses occur at the same times.

Frequency Sweeps.

Next, we turn to the frequency-dependence of the shear and normal stress transfer functions. Their dependence on ω is more complicated than H, yet their behavior again is simply a matter of evaluating the explicit formulas (19,21). Figure 6 shows the result
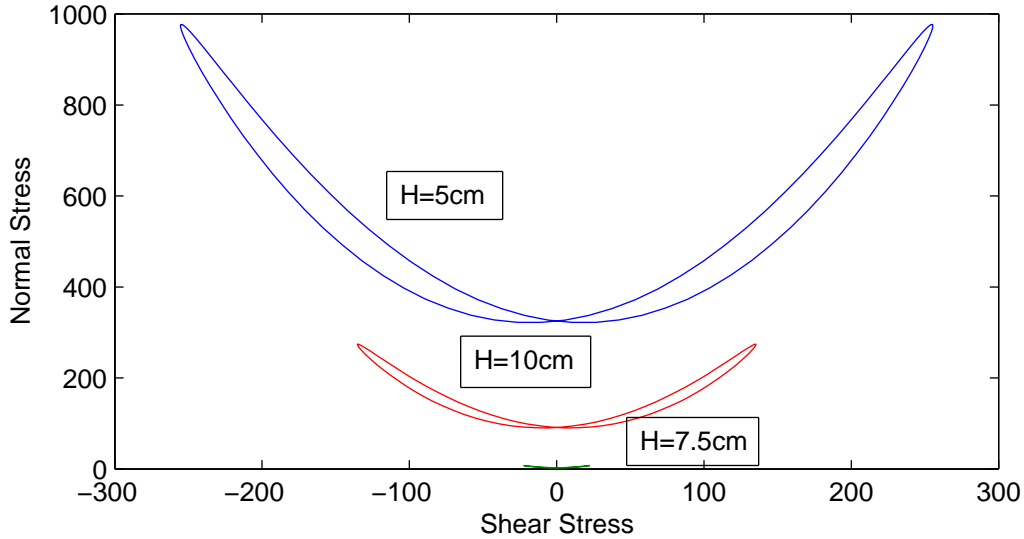
FIGURE 3.6. Time-dependent normal stress versus shear stress loops for Model Fluid 2 for the same data as Figure 4.

for Model Fluid 2 over the frequency range $0 < \omega < 2$ for $H = 10$cm. For the previous H sweep in Figure 2, we fixed $\omega = 1$, and $H = 10$ was near a peak in the shear stress transfer function. From Figure 3.7, it is clear that by increasing or decreasing ω from 1, the extreme interfacial stress functions for normal and shear stress walk off of the peak value, but that additional peaks occur near .5 cm and 1.5 cm. There is no need to restrict to studying the transfer of interfacial stress as a function of a single variable. Figure 3.8 gives the transfer function for extreme interfacial shear stress over several parameters, such as ω and H, with a range of frequency and layer height given by $\omega \in [0, 2]$ and $H \in (0, 10]$ for Model Fluid 2. From graphs such as Figure 3.8, one can find local maxima and minima of the transfer functions over ranges of the driving and fluid parameters.

Scaling behavior for wall extreme values of shear and normal stress.

Before proceeding to the dependence on the UCM material parameters η_0, λ_0 and ρ, we pause to examine the scaling behavior of the oscillatory structure versus H and ω. Namely, the *regularity* of the peaks and valleys versus H and ω is quite striking. From the analysis versus H, it is clear that the behavior is not periodic, except in the elastic limit of $\alpha << \beta$. The elastic solid limit is reached by letting η_0 and λ_0 become large
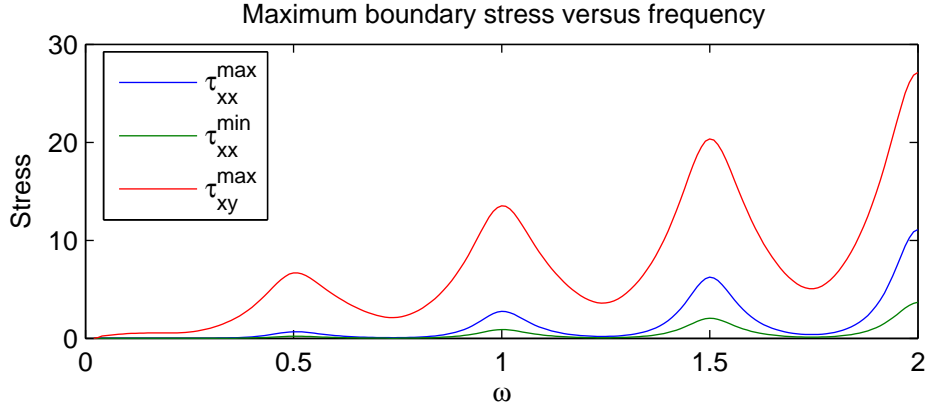
FIGURE 3.7. A frequency sweep of extreme wall shear and normal stresses for Model Fluid 2 over the frequency range $[0, 2]$.
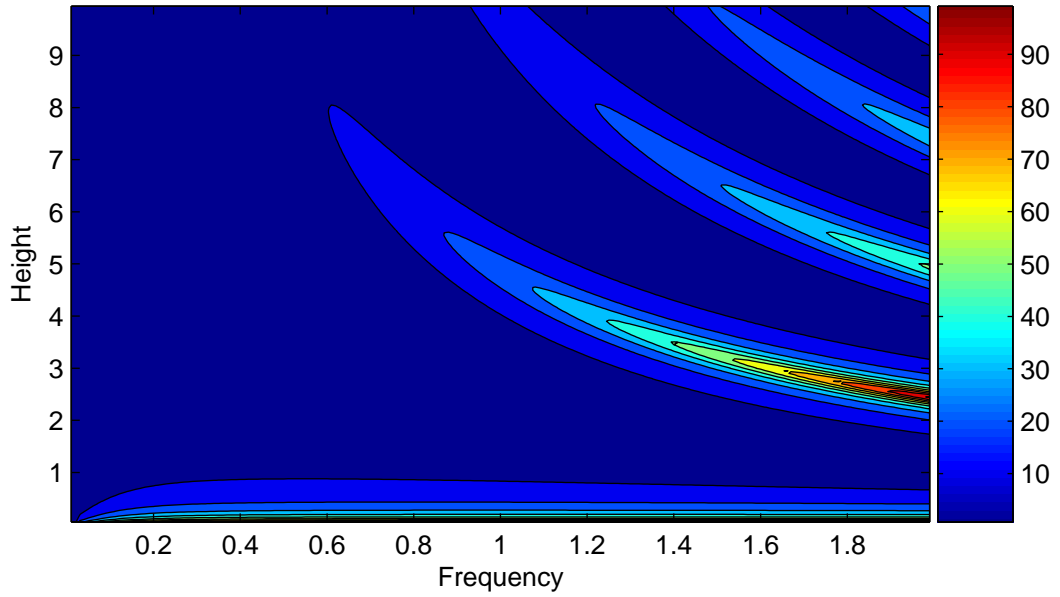

FIGURE 3.8. A parameter sweep of extreme wall shear stress for Model Fluid 2 over the range of parameters $\omega \in [0, 2]$ Hz and $H \in (0, 10]$ cm.

while maintaining a constant ratio. The attenuation and wave length parameters (α and β) become:

$$(3.55) \qquad \lim_{\substack{\eta_0 \to \infty \\ \lambda_0 \to \infty \\ \eta_0/\lambda_0 = c}} \alpha = 0$$

(3.56)
$$\lim_{\substack{\eta_0 \to \infty \\ \lambda_0 \to \infty \\ \eta_0/\lambda_0 = c}} \beta = \omega\sqrt{\rho\lambda_0/\eta_0},$$

and the extreme shear stress transfer function, equation (3.21), becomes,

(3.57)
$$\tau_{xy}^{\max} = V_0 \beta \eta'' |\cot \beta H|.$$

Thus, the extreme shear stress transfer function, in the elastic limit, exhibits asymptotes at,

(3.58)
$$\beta = \frac{\pi}{H}k \qquad k \in \{0, 1, 2, ...\}$$

If we now identify the elastic wave speed,

(3.59)
$$c_0 = \sqrt{\frac{\eta_0}{\lambda_0 \rho}},$$

then β is given by ,

(3.60)
$$\beta = \frac{\omega}{c_0},$$

and thus the resonance condition can be restated in the elastic limit as:

(3.61)
$$\frac{c_0}{2\overline{\omega}H}k = 1 \qquad k \in \{0, 1, 2, ...\},$$

where $\omega = 2\pi\overline{\omega}$. In terms of the frequency sweep, the fundamental frequency, denoted $\overline{\omega}_{\text{fund}}$, becomes

(3.62)
$$\overline{\omega}_{\text{fund}}^{\text{peak}} = c_0/(2H),$$

which is equivalent to a period of plate oscillation that matches the round trip travel time of the elastic shear wave. Additional resonance frequencies are integer multiples of this fundamental frequency. Expressing equation (3.61) with respect to any of the fluid

α/β	H_{fund} Approx	H_{fund} Exact	Percent Error
.000796	.5	.49999	< .00001
.007957	.5	.4999	< .00001
.015913	.5	.4998	.0400
.026515	.5	.4995	.1001
.039726	.5	.4989	.2205
.079075	.5	.4955	.9082
.172598	5	4.819	3.756
.237477	5	4.659	7.319
.552726	5	3.820	30.89

TABLE 1. Errors made when using elastic solid resonance criteria to approximate viscoelastic stress selection criteria.

or control parameters gives a resonance condition for that value. For example,

$$(3.63) \qquad\qquad H_{peak}^{fund} = c_0/(2\overline{\omega}).$$

To extend these results from the elastic solid limit to any viscoelastic fluid, consider the non dimensional parameter α/β. Since $\alpha < \beta$, then for any viscoelastic fluid $\alpha/\beta \in (0,1)$. As we have seen in equations (3.55, 3.56), the elastic solid limit corresponds to $\alpha/\beta = 0$, and further in the viscous limit $\lambda_0 \to 0$ it is clear that $\alpha/\beta = 1$. With respect to this parameter α/β, a measure of where a fluid is in the elastic solid to viscous limit, one could gauge the efficacy of using the elastic solid resonance condition as an estimate for the peaks and valleys of the transfer functions. Table 1 explores the usage of (3.63) as an estimate for the peaks and valleys of the extreme shear stress for a wide range of α/β, and confirms that as $\alpha/\beta \to 1$, the usage of (3.63) as a prediction of the first fundamental peak of the transfer function becomes dramatically worse.

Figure 3.9 gives another interpretation of the data in Table 1, by graphing the percentage error as a function of α/β in the loglog scale. The data points are fit here by a power law, which becomes a line in the loglog scale, and exhibits the nature of the walk off from pure resonance behavior as a fluid deviates from the elastic limit. In summation, for any fluid with known zero shear viscosity η_0 and relaxation time λ_0, one can get an approximation of the fundamental layer height that will maximize stress transfer. The

accuracy of this approximation can be gleaned by from Table 3.1. Further, by solving equation (3.61) for any of the variables, the following approximate scaling conditions (exact in the elastic limit) are identified:

$$(3.64) \qquad\qquad \overline{\omega}^k_{\text{peak}} \approx k c_0 / (2H)$$

$$(3.65) \qquad\qquad H^k_{\text{peak}} \approx k c_0 / (2\overline{\omega})$$

$$(3.66) \qquad\qquad \lambda^k_{\text{peak}} \approx k^2 \frac{1}{4H^2\overline{\omega}^2} \frac{\eta_0}{\rho}$$

$$(3.67) \qquad\qquad \rho^k_{\text{peak}} \approx k^2 \frac{1}{4H^2\overline{\omega}^2} \frac{\eta_0}{\lambda}$$

$$(3.68) \qquad\qquad \eta^k_{\text{peak}} \approx \frac{4H^2\overline{\omega}^2\lambda\rho}{k^2}.$$

Transfer Function Dependence on η_0, λ_0 and ρ.

We now illustrate the inferences gained in the previous section. Namely, there is an underlying oscillatory structure in the extreme values of boundary stresses with respect to all parameters in the model. Figures 3.10-13 show this behavior for the baseline properties of Model Fluid 2 with respect to variations in the elastic relaxation time λ_0, the zero strain rate viscosity η_0 and the fluid density ρ. Note the stress peaks are quite well approximated by the elastic limit scaling behavior presented above, formulas (3.64-68).

3.5. Transfer Function Structure for a Giesekus Fluid

Here we refer to [22] and chapter 1 for a numerical solution to the analogous problem where the constitutive equation is given by a single mode Giesekus model. The boundary stress behavior of this project was, in fact, discovered in this context. Figure 3.13 repeats
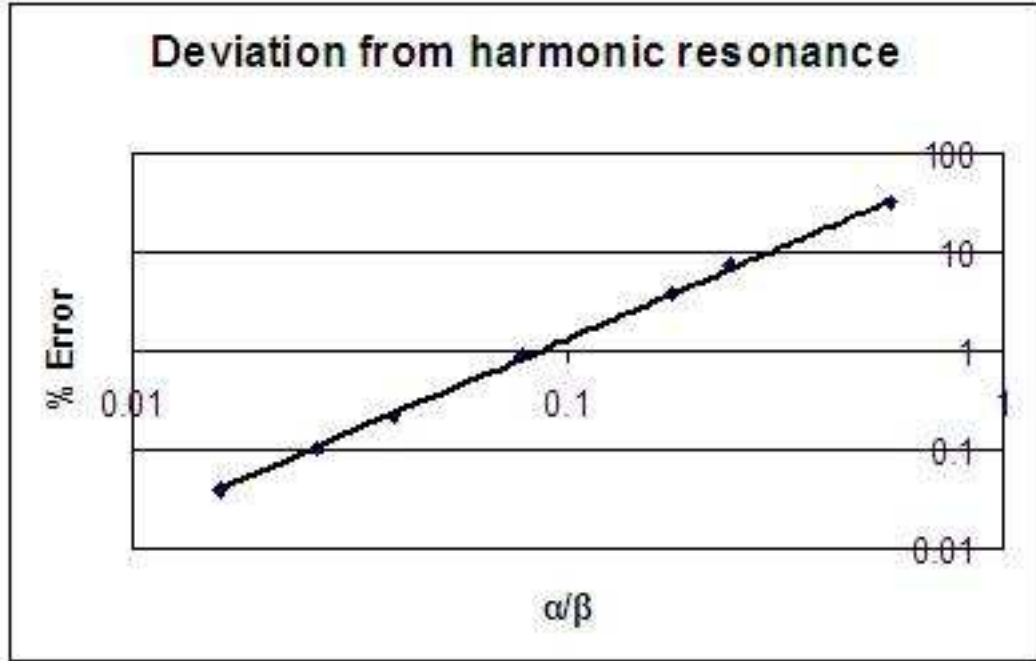
FIGURE 3.9. Percent error calculations for using equation (3.63) to predict peaks of the extreme shear stress for different viscoelastic fluids with given ratios α/β. The scale is loglog and thus the trend-line shown is a simple power law fit to the data.
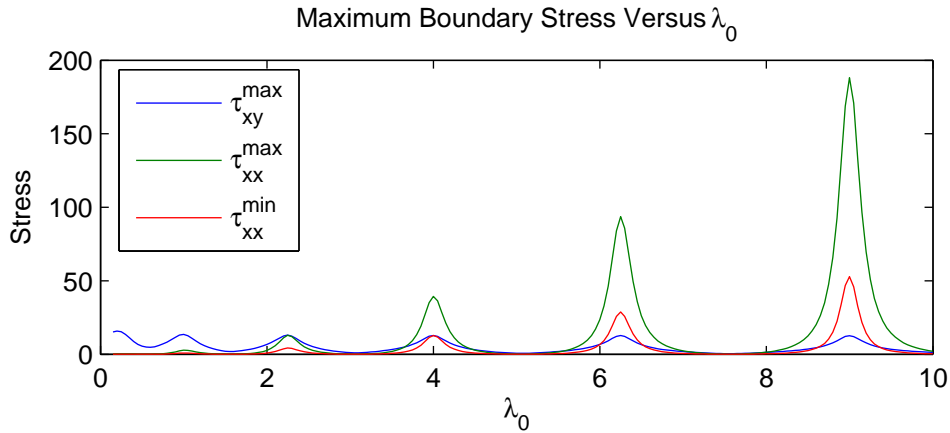

FIGURE 3.10. Relaxation time sweep of extreme boundary shear and normal stresses with respect to λ_0 variations of Model Fluid 2. We fix η_0 and ρ of Model Fluid 2 with boundary values $\omega = 1$ Hz, $A = .1$ cm and $H = 10$ cm then perform a relaxation time sweep. The elastic limit scaling prediction of the kth peak is $\lambda_{peak}^k = .25k^2$.

the H sweep of Figure 3.2 for Model Fluid 2 parameters together with a mobility parameter value of .01. Figure 3.14 shows the result of a frequency sweep, while Figure 3.15
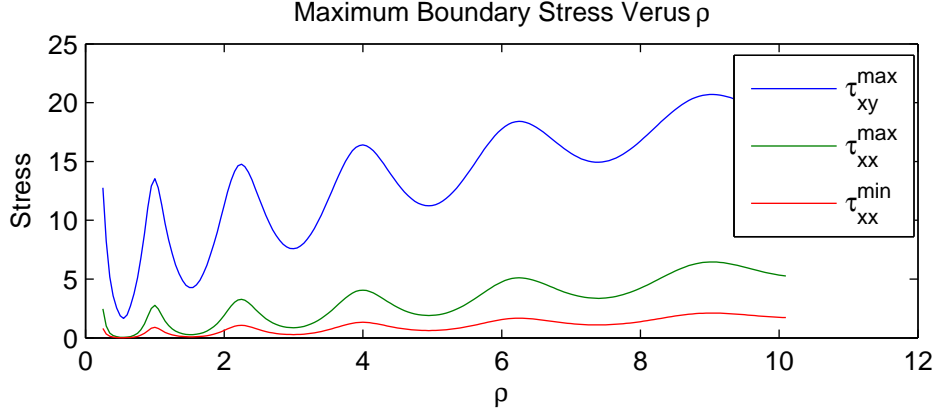
FIGURE 3.11. Density sweep of extreme boundary shear and normal stresses with respect to ρ variations of Model Fluid 2. We fix η_0 and λ_0 of Model Fluid 2 with boundary values $\omega = 1\text{Hz}$, $A = .1$ cm and $H = 10$ cm then perform a density sweep. The elastic limit scaling prediction of the kth peak is $\rho_{peak}^k = .25k^{-2}$.
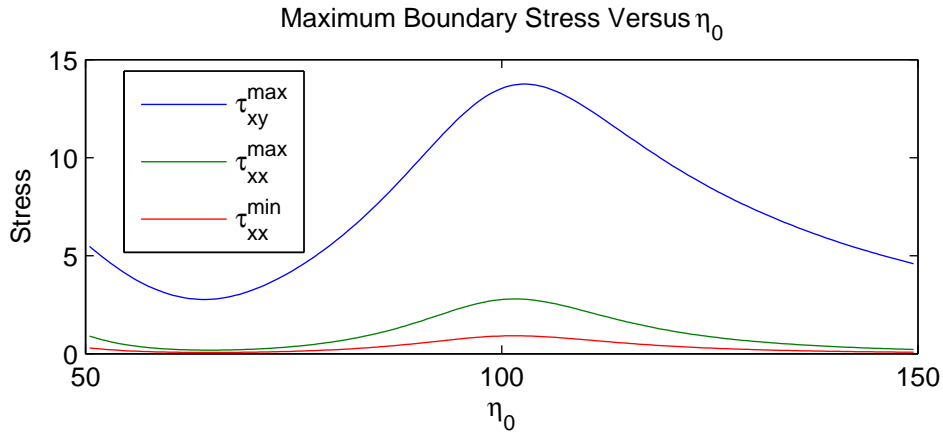

FIGURE 3.12. Zero shear-rate viscosity sweep of extreme boundary shear and normal stresses with respect to η_0 variations of Model Fluid 2. We fix ρ and λ_0 of Model Fluid 2 with boundary values $\omega = 1$ Hz, $A = .1$ cm and $H = 10$ cm then perform a zero shear-rate viscosity sweep. The elastic limit scaling prediction of the kth peak is $\eta_{peak}^k = 400k^{-2}$.

revisits the Lissajous figures of section 3.4.2 and obtains the analogous results for this model. The striking feature of Figure 3.15 is that nonlinearity is evident at $H = 5$ and $H = 10$, but at $H = 7.5$ the fluid exhibits the classic linear behavior (with the elliptical orbit seen in Figure 3.4).
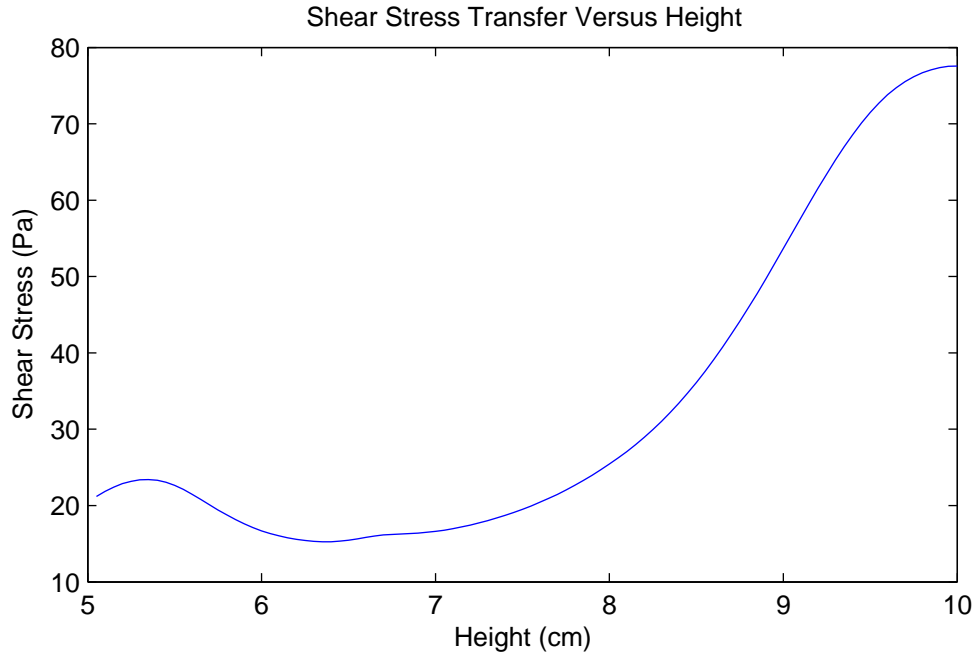
FIGURE 3.13. Maximum shear stress at the lower interface versus channel depth for Model Fluid 2 with a Giesekus mobility parameter of .01. The driving conditions here are $\omega = 1$ Hz and $A = .1$ cm.
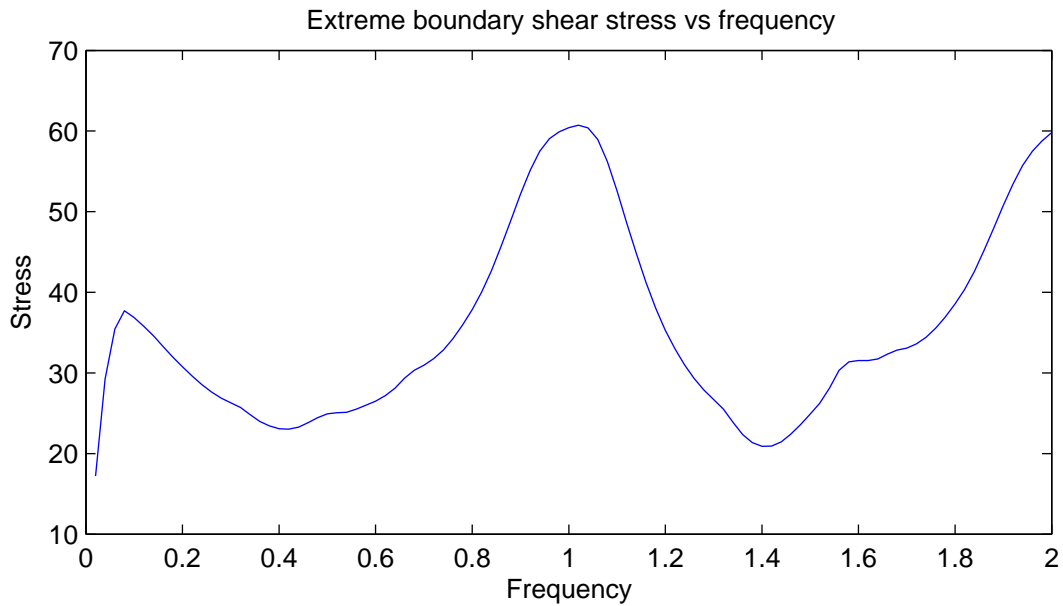

FIGURE 3.14. Maximum shear stress at the lower interface versus frequency for Model Fluid 2 with a Giesekus mobility parameter of .01. The driving conditions here are $\omega = 1$ Hz and $A = .1$ cm.

The pertinent features of Figure 3.13 are that we see a similar height selection mechanism for the transfer of shear stress, and that the figure shows additional nonlinear

structure. Note that the locations of the maxima and minima are notably different. Figure 3.15 contains Lissajous figures for various heights. From the Lissajous figures, it is clear that shear thinning is occurring in the Giesekus fluid at these strains.
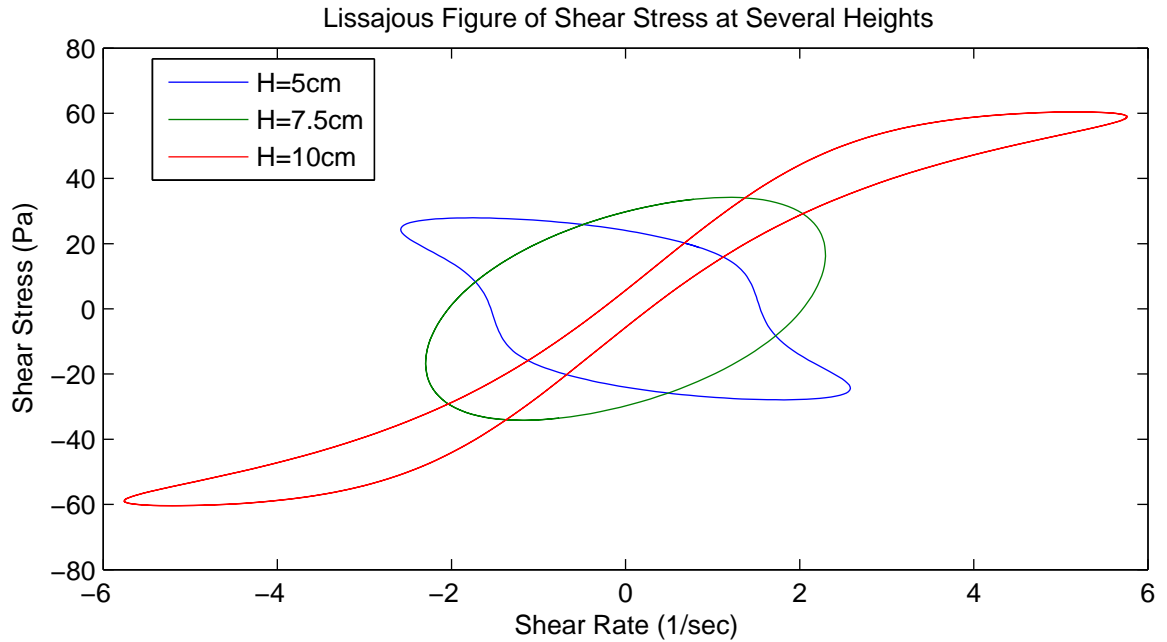

FIGURE 3.15. Shear stress versus shear rate loop for a Giesekus fluid at several heights.

3.6. Stress-controlled versus strain-controlled oscillatory shear

The phenomenon in question has been explored in previous sections for strain-controlled boundary conditions. Alternative boundary conditions, each modeling a different experimental protocol, consist of imposing a periodic stress or strain at either interface. As seen in Chapter 1, any such periodic boundary conditions yield an exact solution, and since stress and strain controlled boundary conditions are equivalent, the phenomenon is persistent. For example, one can impose a periodic shear stress boundary condition at the bottom interface, retaining a stationary top boundary:

(3.69) $$\tau_{xy}(0, t) = \tau_0 \sin(\omega t), \quad v_x(H, t) = 0.$$

It is straightforward to show that this boundary value problem is equivalent to the strain-controlled problem and solution presented above,

$$(3.70) \qquad v_x(y,t) = \mathcal{I}m\left(V_0 e^{i\omega t} \frac{\sinh \delta(H-y)}{\sinh \delta H}\right),$$

where V_0 is now complex valued and given by,

$$(3.71) \qquad V_0 = -\frac{\tau_0}{\eta^* \delta} \tanh \delta H.$$

To relate the complex number V_0 above to its more natural physical interpretation as the maximum imposed velocity of the lower plate, simply take the complex modulus $|V_0|$. In this context, v_x is,

$$(3.72) \qquad v_x(y,t) = \mathcal{I}m\left(|V_0| e^{i(\omega t + \chi)} \frac{\sinh \delta(H-y)}{\sinh \delta H}\right),$$

where $\chi = \arg(V_0)$, demonstrating a clear equivalence of the two stress and strain controlled boundary value problems.

Perhaps more physically interesting (especially for applications to lung biology), is a stress free boundary condition at the upper interface together with an oscillatory strain at the lower interface:

$$(3.73) \qquad v_x(0,t) = V_0 \sin(\omega t), \quad \tau_{xy}(H,t) = 0.$$

The solution is a sum of two solutions of (7-11),

$$(3.74) \qquad v_x(y,t) = \mathcal{I}m\left[e^{i\omega t}\left(V_0 \frac{\sinh \delta(H-y)}{\sinh \delta H} - V_H \frac{\sinh \delta(y)}{\sinh \delta H}\right)\right],$$

where the stress free condition at the upper interface determines V_H,

$$(3.75) \qquad V_H = V_0 \operatorname{sech}(\delta H).$$

Figure 3.16 gives a snapshots of shear waves with the stress free upper boundary condition. Finally, Figure 3.17 gives the analogous height sweep versus extreme boundary
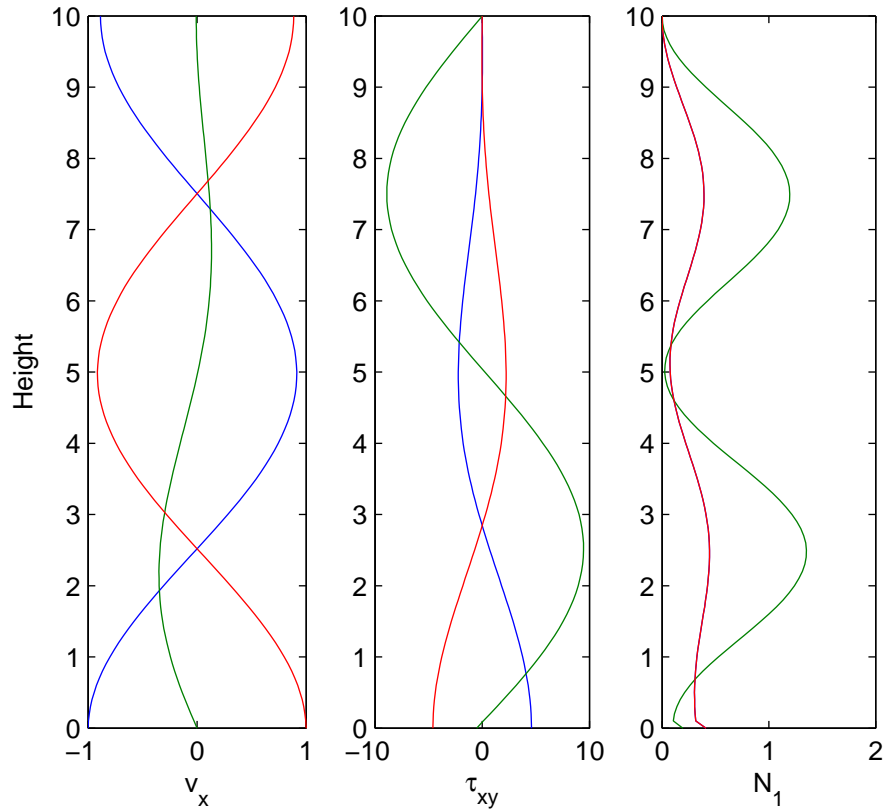
FIGURE 3.16. Snapshots of shear waves with a stress free upper interface. Fluid values here are Model Fluid 2, and driving conditions are $V_0 = 1$ cm/sec, $\omega = 1$ Hz. The blue, green, and red lines indicates snapshots at $t = 19.75$, $t = 20$, and $t = 20.25$ sec respectively.
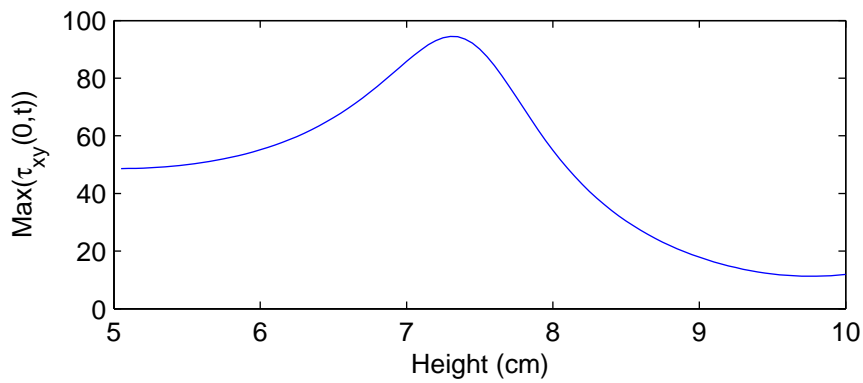

FIGURE 3.17. Channel depth parameter sweep for oscillating lower boundary, stress free upper boundary. Fluid values here are Model Fluid 2, and driving parameters are the same as those used in earlier figures.

shear stress for a single mode Maxwell fluid with a stress free upper interface. Using a

similar approach, one can determine solutions for all four sets of well-posed boundary conditions. Clearly the phenomenon persists.

3.7. Conclusion

The response of a viscoelastic layer in oscillatory shear has been explored with a focus on the extreme values of boundary stress signals. The phenomenon we have identified is an oscillatory structure in boundary stress signals with respect to all parameters (layer thickness, frequency of imposed shear, or material properties). This structure indicates a redundant mechanism with which to either communicate stress signals, by tuning to the peaks of the structure, or to filter stress by tuning to the valleys. Using the upper convected Maxwell model, we provide a rigorous explanation of the phenomenon, and then illustrate its persistence with a Giesekus model simulation where the results were first discovered. The relevance of these results to the biological setting of ciliary transport of mucus layers remains for future studies. The implication we have in mind is the ability of epithelial cells or cilia to mechanically sense perturbations in normal homeostatic conditions, through the variability in stress signals shown here. These perturbations may arise from mucus layer thickness variations or changes in material properties due to hydration or perhaps due to a significant deposition of pathogens at the air-mucus interface.

BIBLIOGRAPHY

1. D.M. Bates & D.G. Watts **Nonlinear Regression Analysis and Its Applications,** Wiley, New York, (1988)

2. R. Bird, C. Curtis, R. Armstrong & O. Hassenger, **Dynamics of Polymer Fluids**, vol. 1 & 2, 2nd ed., Wiley, New York, 1987.

3. A. I. Barakat, D. K. Lieu, & Andrea Gojova, *Ion channels in shear stress sensing in vascular endothelium,* from **Molecular Sensors for Cardiovascular Homeostasis**, Springer US, p 155-170, 2007.

4. B. Button, M. Picher, R. C. Boucher, *Differential effects of cyclic and constant stress on ATP release and mucociliary transport by human airway epithelia*, J. Physiol., 580(2), 577-592, 2007.

5. M. W. Denny, *Mechanical properties of pedal mucus and their consequences for gastropod structure and performance,* Amer. Zoologist, 24(1), 23-36, 1984.

6. R.H. Ewoldt, A. E. Hosoi and G. H. McKinley. *Rheological Fingerprinting of Complex Fluids using Large Amplitude Oscillatory Shear (LAOS) Flows,* Nordic Rheology Conference, Stavanger, Norway, Annual Transactions of the Nordic Society of Rheology pp. 3-8 (2007)

7. R.H. Ewoldt, C. Clasen, A.E. Hosoi, and G.H. McKinley, *Rheological fingerprinting of gastropod pedal mucus and synthetic complex fluids for biomimicking adhesive locomotion,* Soft Matter 3(5), 634-643, 2007

8. R. H. Ewoldt, A. E. Hosoi, and G. H. McKinley, *Rheology of mucin films for molluscan adhesive locomotion,* Abstr. Pap. Am. Chem. Soc. 231(387-PMSE), 2006

9. J. D. Ferry, *Studies of the Mechanical Properties of Substances of High Molecular Weigh I. A Photoelastic Method for Study of Transverse Vibrations in Gels,* Rev. Sci. Inst., Vol.12, 79-82, (1941)

10. J. D. Ferry, *Behavior of Concentrated Polymer Solutions under Periodic Stresses,* J. Polym. Sci, 2:593-611, (1947)

11. J. D. Ferry, F.T. Adler, & W.M. Sawyer *Propagation of Transverse Waves in Viscoelastic Media,* J. Appl. Phys., 20, 1036-1041, (1949)

12. D.B. Hill, B. Lindley, M.G. Forest, R. Superfine, & S.M. Mitran *Experimental and modeling protocols from a micro-parallel plate rheometer,* UNC Preprint, 2008

13. D.B. Hill, R. Superine, *Microbead Rheology*, in preparation.

14. R.S. Jeyaseelan & A.J. Giacomin *Network theory for polymer solutions in large amplitude oscillatory shear,* J. Non-Newtonian Fluid Mech., 148 (1), p.24-32, Jan 2008.

15. R. Keunings & K. Atalik *On the occurrence of even harmonics in the shear stress response of viscoelastic fluids in large amplitude oscillatory shear,* J. Non-Newtonian Fluid Mech., 122, 107-116, (2004).

16. R.G. Larson, **Constitutive Equations for Polymer Melts and Solutions**, Out of Print. Copies Available via personal contact rlarson@umich.edu

17. R. J. Leveque, CLAWPACK - Conservation Law Package, http://www.amath.washington.edu/∼claw

18. R. J. Leveque, *Wave propagation algorithms for multi-dimensional hyperbolic systems*, J. Comp. Phys., 131, 327-353, 1997.

19. B. Lindley, E.L. Howell, B. Smith, G. Rubinstein, M.G. Forest, S. Mitran, *Stress communication and filtering of viscoelastic layers in oscillatory shear* Submitted, J Non-Newtonian Fluid Mech., (2008)

20. L. Mahadevan, S. Daniel, & M. K. Chaudhury, *Biomimetric ratcheting motion of a soft, slender, sessile gel*, P. Natl. Acad. Sci, 101(1), 23-26, 2003.

21. H. Matsui, S. Randell, S. Peretti, C. W. Davis, & R. C. Boucher, *Coordinated clearance of periciliary liquid fand mucus from airway surfaces,* J. Clin. Invest., 102(6), 1125-1131, 1998.

22. S.M. Mitran, M.G. Forest & et. al. *Extenstions of the Ferry shear wave model for active linear and nonlinear microrheology,* J. Non-Newtonian Fluid Mech., to appear, (2008)

23. S.M. Mitran, *Highly Accurate Solutions of the non-linear and one-dimensional viscoelastic shear wave problem for Giesekus type fluids,,* (in preparation)

24. S.M. Mitran, BEARCLAW - A software frame-work multiphysics numerical simulation, http://www.amath.unc.edu/Faculty/mitran/bearclaw.html.

25. L. Preziosi , *On an invariance property of the solution to Stokes first problem for viscoelastic fluids* J. Non-Newtonian Fluid Mech., 33 (2), p.225-228, Jan 1989

26. L. Preziosi, D.D. Joseph,*Stokes' first problem for viscoelastic fluids,* J. Non-Newtonian Fluid Mech., 25 (3), p.239-259, Jan 1987

27. M. N. Surya, Y. Kawanabe, J. J. Kaminski, W. J. Pearce, D. E. Ingber, J. Zhou, *Endothelial Cilia are fluid shear sensors that regulate calcium signaling and nitric oxide production through polycystin-1*, Circulation, 117, 1121-1123, 2008.

28. R. Tarran, B. R. Grubb, J. T. Gatzy, C. W. Davis & R. C. Boucher, *The relative roles of passive surface forces and active ion transport in the modulation of airway surface liquid volume and composition*, J. Gen. Phys., Vol. 118(2), 223-236, 2001.

29. R. Tarran , B. Button, M. Picher, A. M. Paradiso, C. M. Ribeiro, E. R. Lazarowski, L. Zhang , P. L. Collins, R. J. Pickles, J. J. Fredberg, R. C. Boucher, *Normal and cystic fibrosis airway surface liquid homeostasis. The effects of phasic shear stress and viral infections.* J. Biol. Chem. 280(42):35751-9, 2005.

30. T.T. Tee, J.M. Dealy, *Nonlinear Viscoelasticity of Polymer Melts,* Trans. Soc. Rheol. 19, 595-615, (1975)

31. G. B. Thurston, J. L. Schrag, *Shear wave propagation in a Birefringent viscoelastic media*, J. Appl. Phys. 35, 144, 1964.

32. http://www.amath.unc.edu/Faculty/mitran/research/viscelas/ shear1d.xhtml